13. VALIK MEETODEID II

13.1 Numbrilised meetodid

häiritusmeetod

Runge-Kutta meetod

lõplike vahede meetod

lõplike elementide meetod

spektraalanalüüs

13.2 Spetsiifilised meetodid

Petri võrgud

närvivõrgud

fraktaalgeomeetria

D.P. Atherton, P.Borne

Concise Encyclopedia of Modelling and Simulation

Pergamon Press, Oxford, 1992

13.1 Numbrilised meetodid

Vaja lahendada:

- algebralised võrrandid / süsteemid;
- harilikud diferentsiaalvõrrandid / süsteemid;

  lineaarsed;

  mittelineaarsed;
- osatuletistega diferentsiaalvõrrandid / süsteemid;
- integralvõrrandid;

  jne.

Kasutusel matemaatikapaketid

Matlab, Maple, Mathematica, …

13.1 Numbrilised meetodid

Harilikud diferentsiaalvõrrandid

$$\frac{d^2y}{dt^2} + a\frac{dy}{dt} + b\,y = 0$$

analüütiliselt lahendatav

$$\frac{d^2y}{dt^2} + a\frac{dy}{dt} + by^n = 0, \qquad n = 2,3,4,...$$

? Vt. Kamke käsiraamat
numbrilised meetodid

Häiritusmeetod, kui esineb väike parameeter ε

$$\frac{d^2f}{dt^2} + f = -\varepsilon f^3$$ (Duffingi võrrand)

$$f(t;\varepsilon) = \sum_{n=0}^{\infty} \varepsilon^n\, f_n(t)$$

$$\varepsilon^0, \quad \varepsilon^1, \quad \varepsilon^2, ...$$

$$\theta(\varepsilon^0): \frac{d^2f_1}{dt^2} + f_0 = 0$$

$$\theta(\varepsilon^1): \frac{d^2f_1}{dt^2} + f_1 = -f_0^3$$

$$\theta(\varepsilon^2): \frac{d^2f_2}{dt^2} + f_2 = -3f_0^2\, f_1$$

Vt. Levin–Ulm

Runge – Kutta meetod

$$\frac{dy}{dt} = f(y,t)$$

Idee:

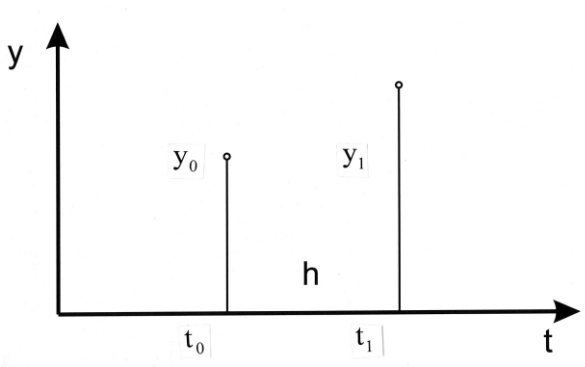

$y_0\,(t_0)$ antud, leida $y_1\,(t_1)$, $y_2\,(t_2)$, …

samm h tuleb valida

$$\frac{y_1 - y_0}{h} = f(y_0, t_0)$$

Esimest järku lähendus (lihtsaim)

$$y_1 = y_0 + h\,f(y_0, t_0)$$

Teist järku lähendus

$$y_1 = y_0 + h\,f\left(t_0 + \frac{h}{2},\quad y_0 + \frac{h\,f(y_0,t_0)}{2}\right)$$

. . . .

Vt. matemaatikapaketid

Faasiruum – muutujate ruum

$$\frac{dx}{dt} = f(x, y) \qquad \frac{dy}{dt} = g(x, y)$$

x (t), y (t); {x, y} - muutujate ruum

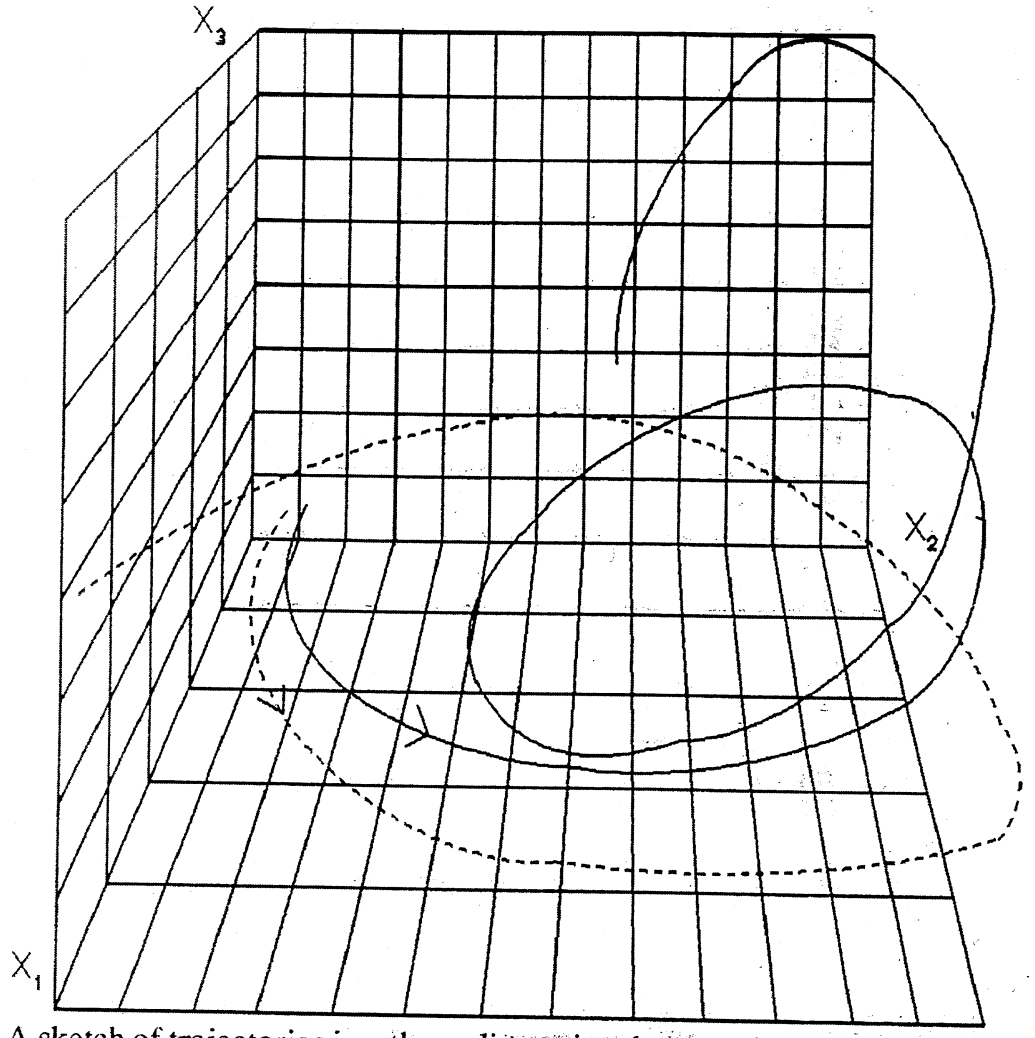

A sketch of trajectories in a three-dimensional state space. Notice how two nearby trajectories, starting near the origin, can continue to behave quite differently from each other yet remain bounded by weaving in and out and over and under each other.

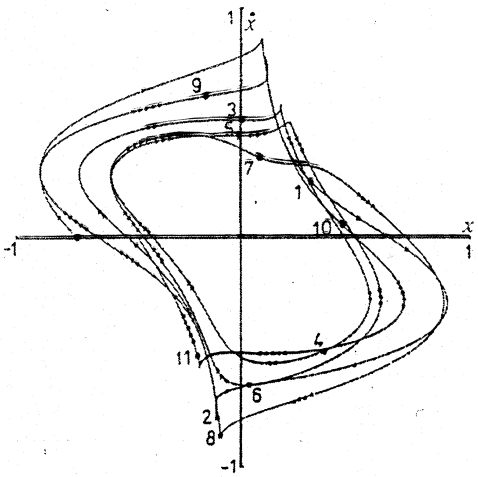

Süsteemi $\ddot{x} + g(x, \dot{x}) = f(t)$ Poincaré lõike nummerdatud punktid $x, \dot{x}$-tasandil. *Thompson, Stewart, 1986.*

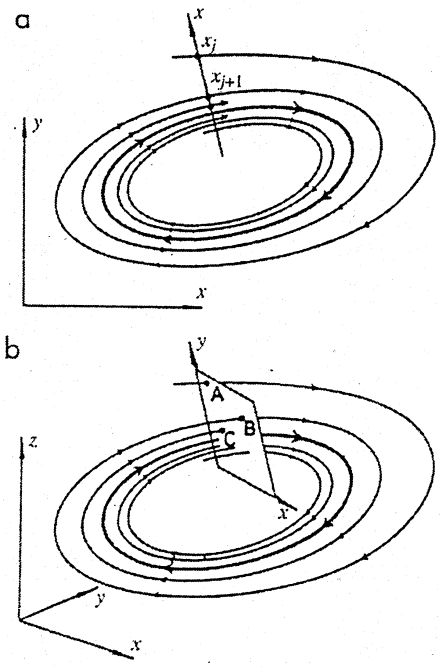

(a) ühedimensionaalne Poincaré lõige; (b) kahedimensionaalne Poincaré lõige. *Thompson, Stewart, 1986.*

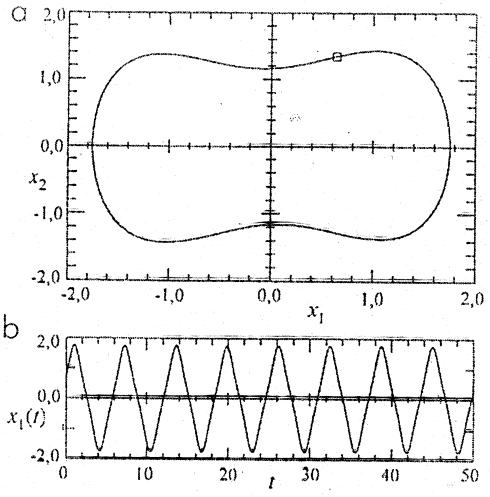

Ühekordselt perioodiline liikumine: (a) faasikõver; (b) aja-tee diagramm. *Verhulst, 1990.*

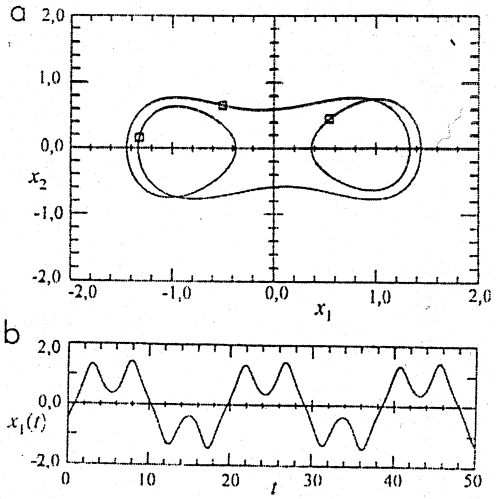

Mitmekordselt perioodiline liikumine: (a) faasikõver; (b) aja-tee diagramm. *Verhulst, 1990.*

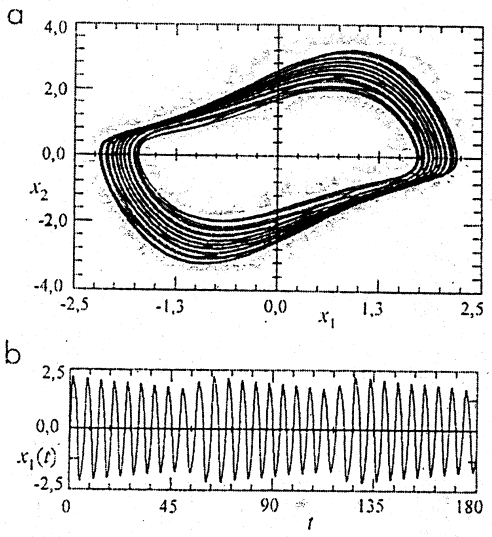

Kvaasiperioodiline liikumine: (a) faasikõver; (b) aja-tee diagramm. *Parker, Chua, 1989.*

$$G_1(x,y,z) = -\sigma x + \sigma y \ ,$$
$$G_2(x,y,z) = -y + rx - xz \ , \qquad (12)$$
$$G_3(x,y,z) = -bz + xy \ ,$$

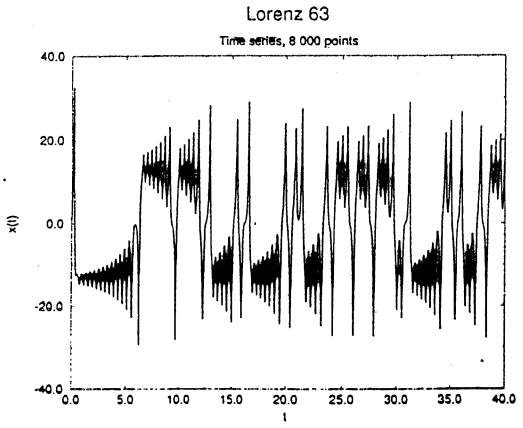

FIG. 1. Chaotic time series $x(t)$ produced by Lorenz (1963) equations (11) with parameter values $r=45.92$, $b=4.0$, $\sigma=16.0$.

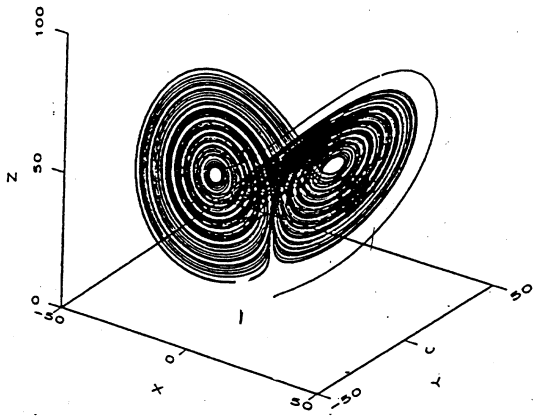

FIG. 2. Lorenz attractor in three-dimensional phase space $(x(t),y(t),z(t))$.

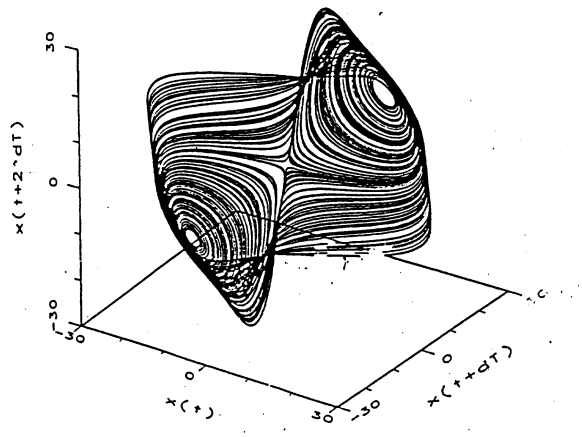

FIG. 7. Lorenz time series $x(t)$ (Fig. 1) embedded in a three-dimensional phase space $(x(t),x(t+dT),x(t+2dT))$, $dT=0.2$.

Lõplike vahede meetod

Idee - asendada tuletised lõplike vahedega

1 D

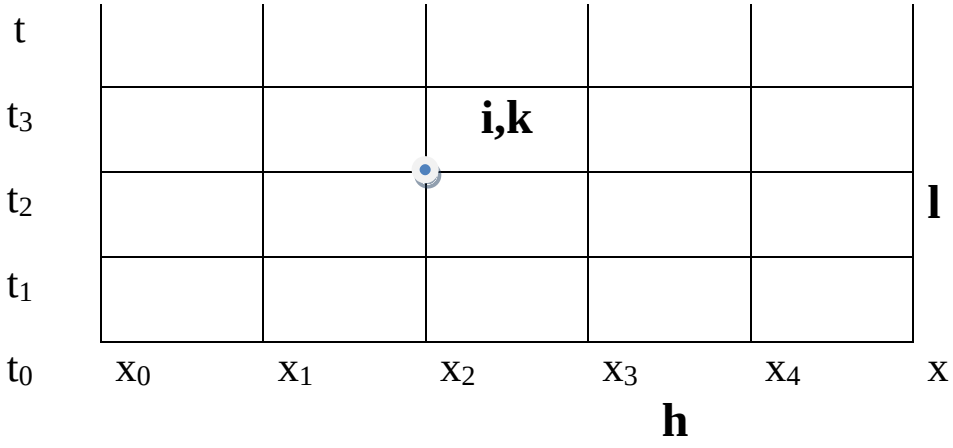

Näide: lainevõrrand

$$\frac{\partial^2 u}{\partial t^2} = a^2 \frac{\partial^2 u}{\partial x^2}, \qquad a = \text{const}$$

$$\frac{\partial u}{\partial t} = \frac{u_{i,k+1} - u_{i,k}}{l}$$

$$\frac{\partial^2 u}{\partial t^2} = \frac{u_{i,k+1} - 2u_{i,k} + u_{i,k-1}}{l^2}$$

$$\frac{u_{i,k+1} - 2u_{i,k} + u_{i,k-1}}{l^2} = a^2 \frac{u_{i+1,k} - 2u_{i,k} + u_{i-1,k}}{h^2}$$

täpsuse küsimus oluline

ilmutatud, ilmutamata süsteemid

Lõplike vahede meetod – näide

$$\frac{\partial \mathbf{W}}{\partial t}+\frac{\partial \mathbf{F}(\mathbf{W})}{\partial x}+\mathbf{C}(\mathbf{W})=0, \tag{1}$$

where W, F, C defined as

$$\mathbf{W}(x,t)=\begin{bmatrix}\rho\\ \rho u\\ \rho e_0\end{bmatrix},\quad \mathbf{F}(\mathbf{W})=\begin{bmatrix}\rho u\\ \rho u^2+p\\ \rho u h_0\end{bmatrix},$$

$$\mathbf{C}(\mathbf{W})=\begin{bmatrix}\rho u\\ \rho u^2\\ \rho u h_0\end{bmatrix}\frac{1}{S}\frac{dS}{dx}+\begin{bmatrix}0\\ \rho G\\ -\rho q\end{bmatrix} \tag{2}$$

The two-step Lax–Wendroff method calculates the vector $\mathbf{W}^{n+1}$ at time t_{n+1} at the node i from the known vectors $\mathbf{W}^n$, $\mathbf{F}^n$, $\mathbf{C}^n$ in the nodes $i-1, i, i+1$ (three-point stencil) at time t_n, by means of two succeeding steps [Fig. 2(a)]. First, $\mathbf{W}^{n+1/2}$ is computed at the intermediate nodes $i-1/2, i+1/2$ at time $t_{n+1/2}$ (forward in time of $\Delta t/2$):

$$\mathbf{W}_{i+1/2}^{n+1/2}=\frac{1}{2}(\mathbf{W}_{i+1}^n+\mathbf{W}_i^n)-\frac{\Delta t}{2\Delta x}(\mathbf{F}_{i+1}^n-\mathbf{F}_i^n)$$
$$-\frac{\Delta t}{4}(\mathbf{C}_{i+1}^n+\mathbf{C}_i^n) \tag{3}$$

$$\mathbf{W}_{i-1/2}^{n+1/2}=\frac{1}{2}(\mathbf{W}_i^n+\mathbf{W}_{i-1}^n)-\frac{\Delta t}{2\Delta x}(\mathbf{F}_i^n-\mathbf{F}_{i-1}^n)$$
$$-\frac{\Delta t}{4}(\mathbf{C}_i^n+\mathbf{C}_{i-1}^n) \tag{4}$$

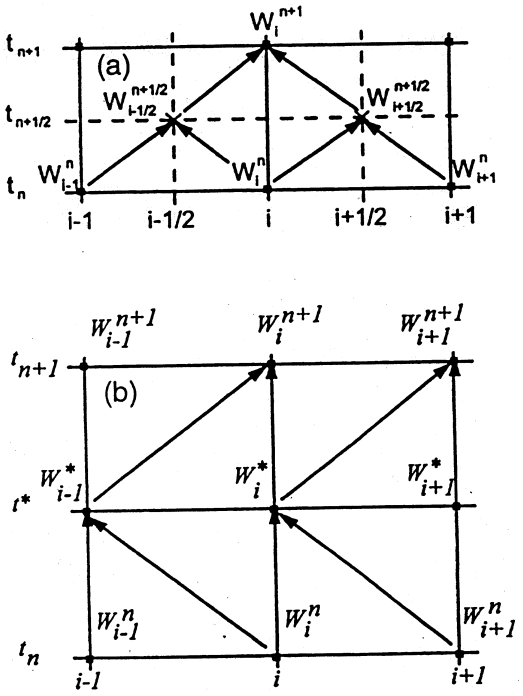

Fig. 2 – Distance–time plane for the two-step Lax–Wendroff method (a) and the MacCormack predictor–corrector method (b).

Lõplike elementide meetod

Idee: kõik funktsioonid aproksimeeritakse diskreetsetena teatud elementide punktides. Elementide valik sõltub probleemi geomeetriast.

Tüüpiline element: kolmnurk

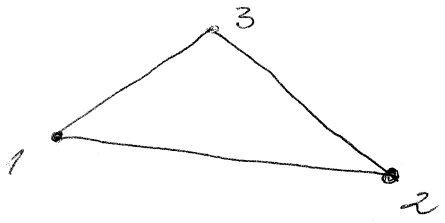

Funktsioon aproksimeeritakse sõlmedes 1, 2, 3

Täpsuse tõstmiseks:

- väiksem element
- täpsem interpolatsioon

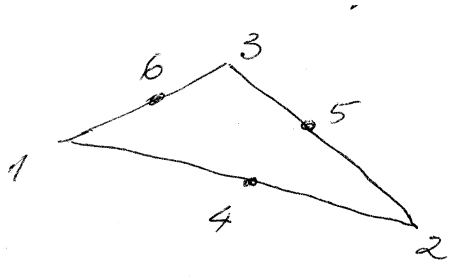

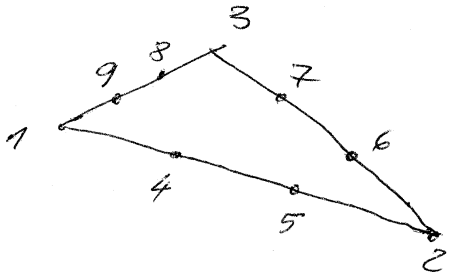

Ruumilised elemendid

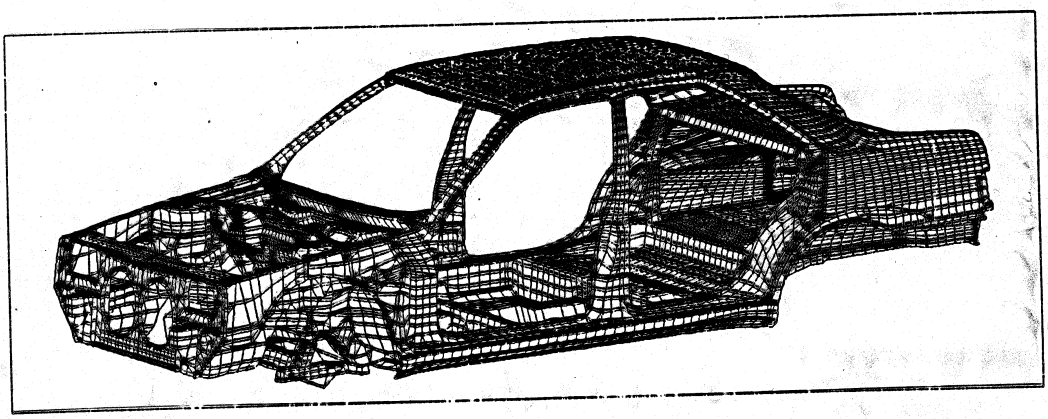

Figure 2 - Maillage utilisé pour l'étude d'une structure en construction automobile (document communiqué par Peugeot S.A.).

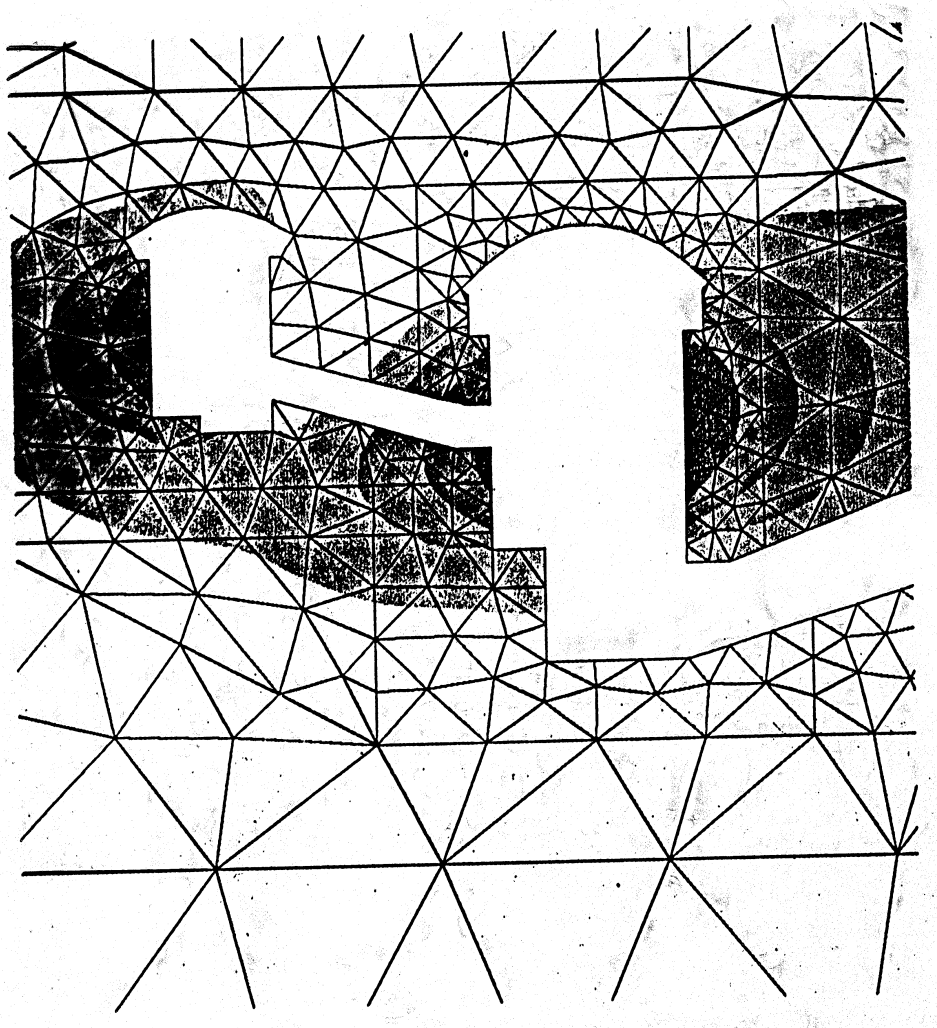

Figure 3 - Centrale hydroélectrique de Long Tan (République populaire de Chine) : effet du creusement. L'intensité de la couleur visualise l'amplitude du déplacement. Etude effectuée par le Laboratoire central des ponts et chaussées pour E.D.F.).

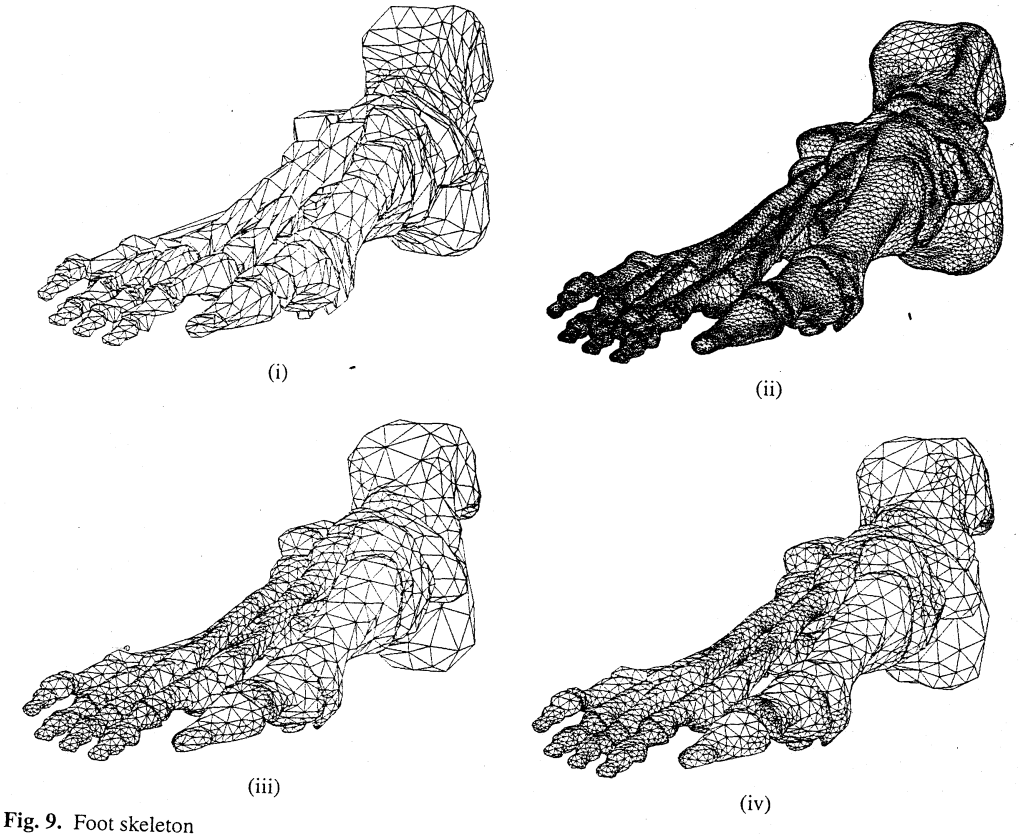

Fig. 9. Foot skeleton

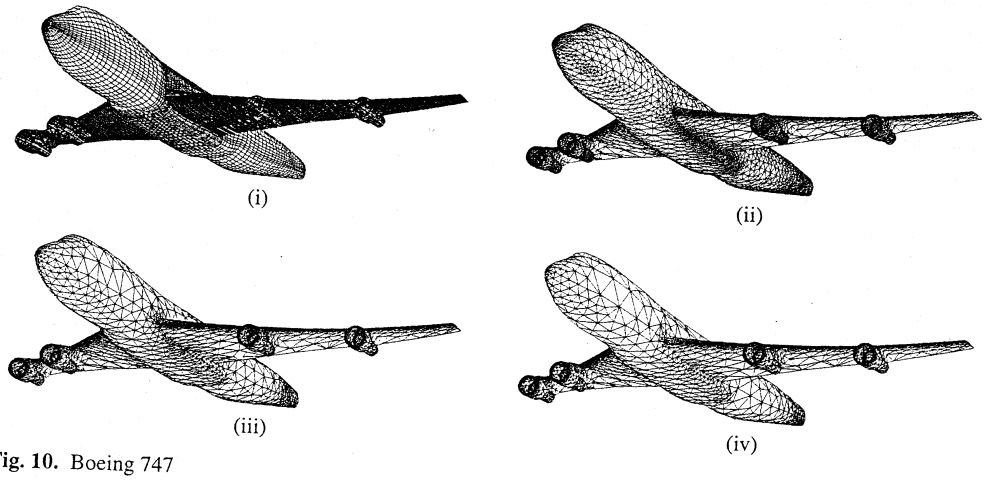

Fig. 10. Boeing 747

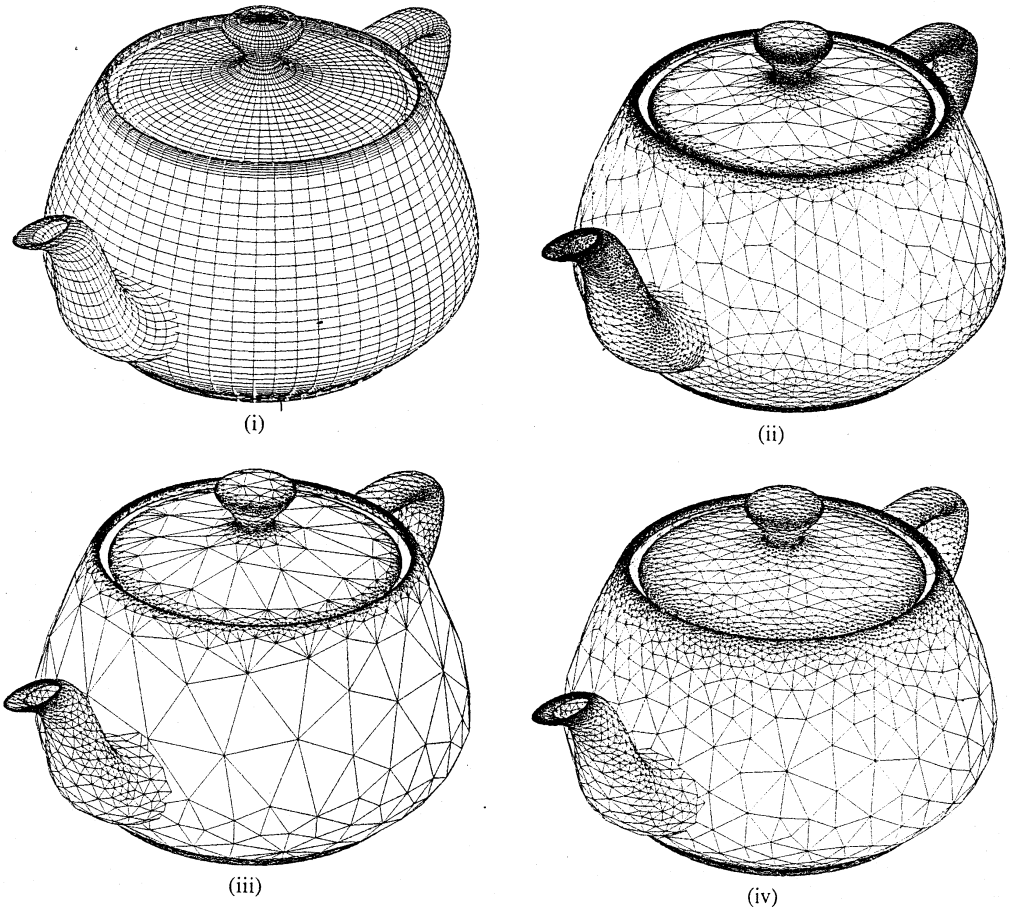

Fig. 7. Utah teapot

Spektraalanalüüs

Lineaarsed võrrandid

$$\varphi_{tt} + \gamma \varphi_{xxxx} = 0$$

$$\varphi_{tt} - \alpha^2 \varphi_{xx} = \beta^2 \varphi_{xxtt}$$

. . .

$$\varphi = \int_0^\infty F(k) \cos(k\,x - \omega\,t)\,dk$$

k – lainearv
ω – sagedus
F(b) – dispersioonifunktsioon
F(k) alg – ja ääretingimuste rahuldamine

Lahend: üksikute harmooniliste lainete summa
igal erinev lainearv

Faasikiirus

$$c_f(k) = \frac{\omega(k)}{k}$$

Grupikiirus

$$c_g(k) = \frac{d\omega}{dk}$$

Näide

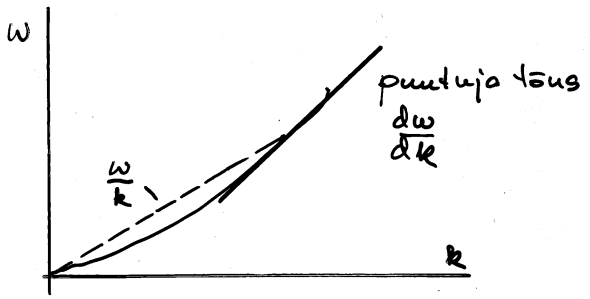

Spektraalmeetodil arvutatud solitonide interaktsioonipilt

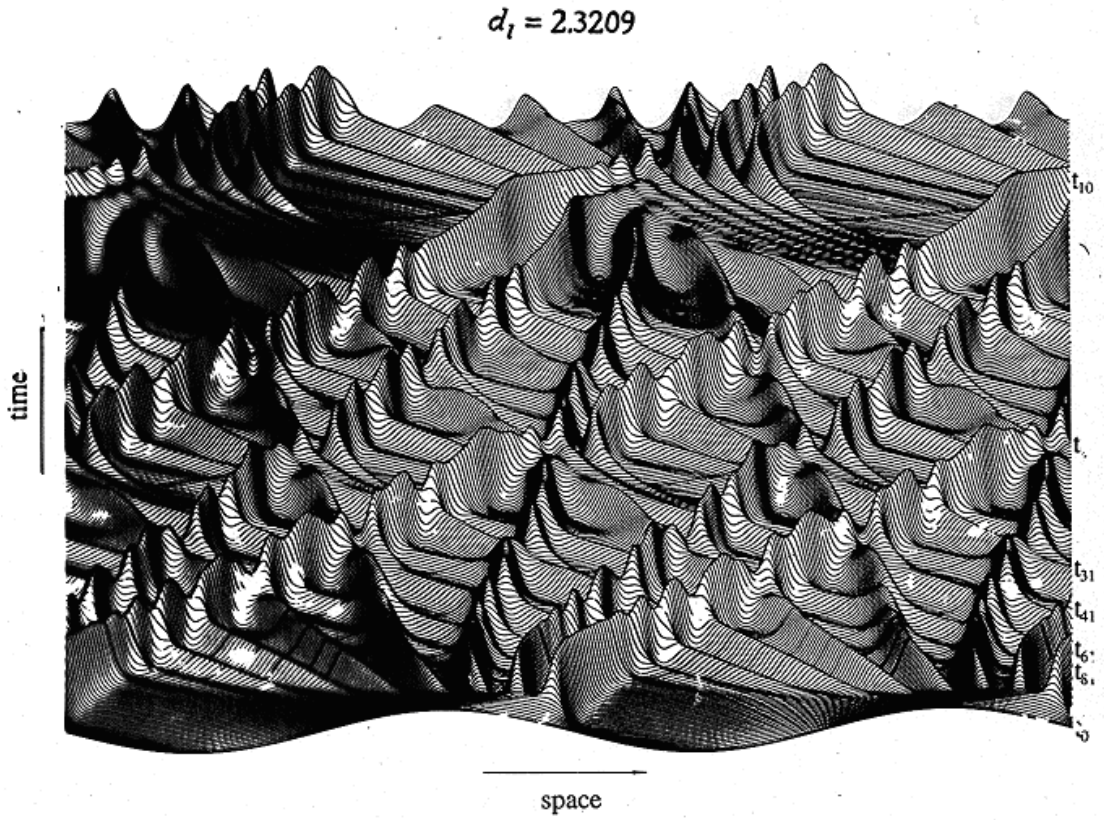

Time-slice plot
Bold lines indicate the profiles corresponding to certain t_i's or t_{ij}'s

KdV $d_t = 1.6$

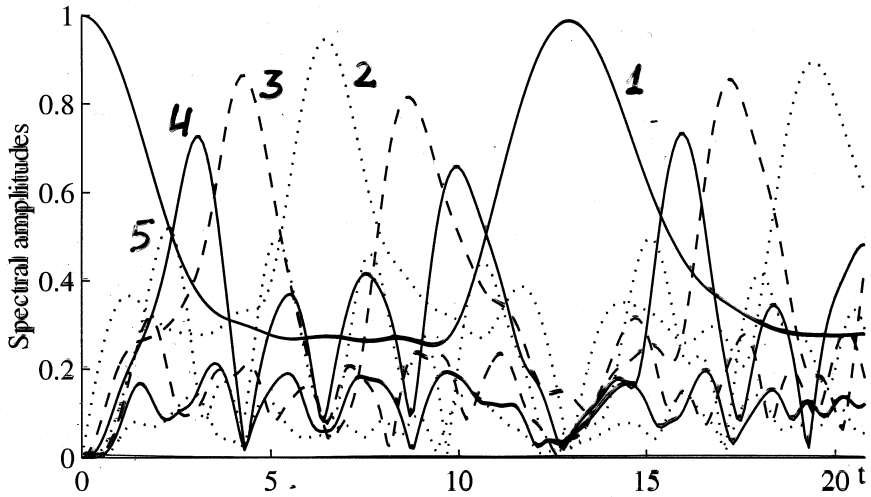
Spectral amplitudes
1
0.8
0.6
0.4
0.2
0
0
5
10
15
20
t
1
2
3
4
5

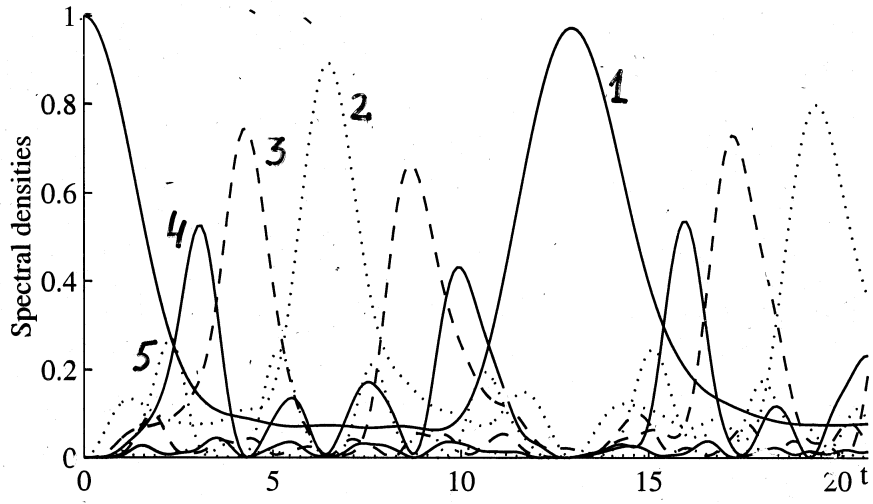
Spectral densities
1
0.8
0.6
0.4
0.2
0
0
5
10
15
20
t
1
2
3
4
5

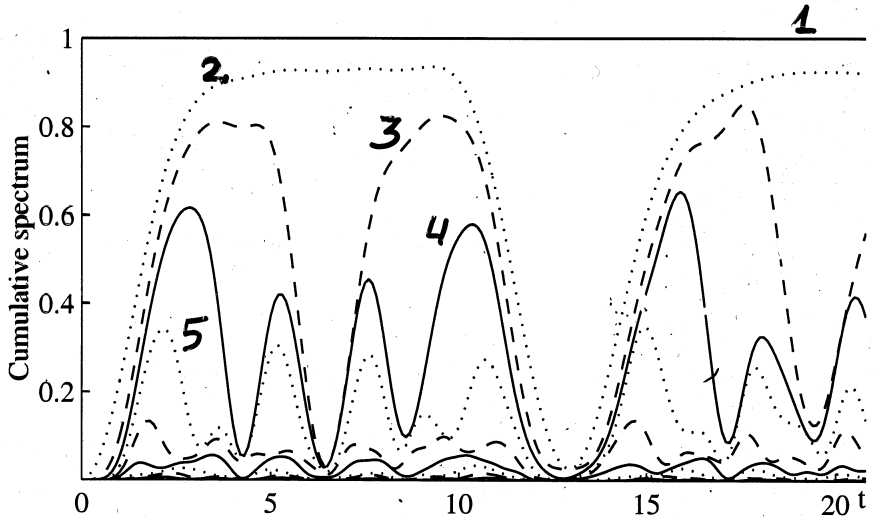
Cumulative spectrum
1
0.8
0.6
0.4
0.2
0
5
10
15
20
t
1
2
3
4
5

13.2 Spetsiifilised meetodid

Petri võrgud

Graafmudel, mis sobib üheaegselt (paralleelselt) toimuvate protsesside kirjeldamiseks

- arvutite tarkvara;
- infosüsteemid;
- protsesside juhtimine (tehnoloogia);
- juriidilised süsteemid;
- …

Suunaga graaf, millel on koht ja ülekanne

Näide protsessi algus

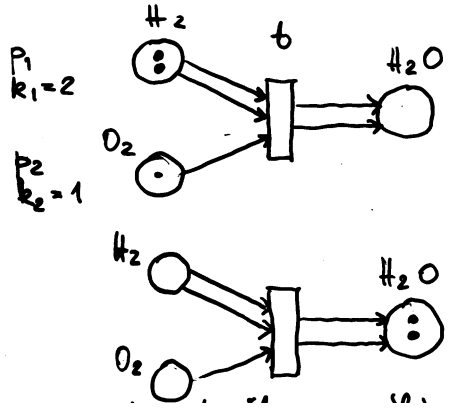

protsessi lõpp

sisend ülekanne väljund

Tähistus: koht p on k väärtust (vt punktid!)

Reeglid:

1) Ülekanne t on võimalik kui iga sisendi koht p on tähistatud sama paljude väärtusega kui palju on ühendusi p ülekandeni *t.*

2) Ülekande sooritus tähendab, et üks väärtus k ühe ühenduse kohta kaob sisendist ja üks väärtus k ühe ühenduse kohta tekib väljundis.

Probleem: Hiina filosoofid

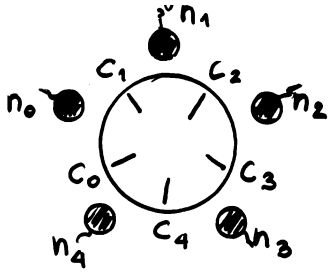

Petri võrgu esitus Olemasolevad

Mõtlemine pulgad

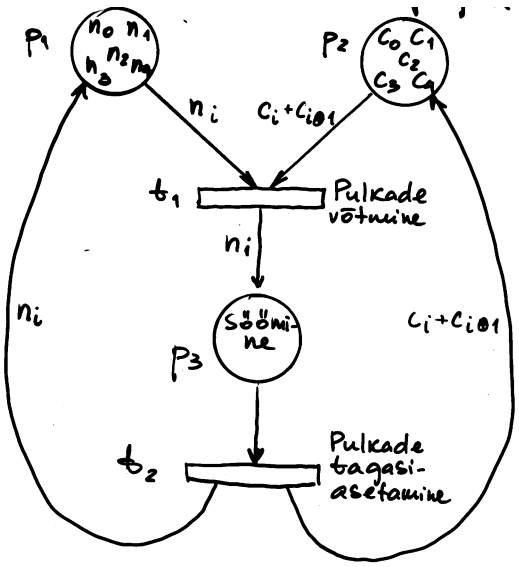

θ1 mooduli 5 lisamine

Iseloomustav maatriks A – ülekannete arv

$$\begin{array}{c} \\ t_1 \\ t_2 \end{array} \begin{array}{c} \begin{array}{ccc} p_1 & p_2 & p_3 \end{array} \\ \begin{vmatrix} -n_i & -c_i - c_{i01} & n_i \\ n_i & c_i + c_{i01} & -n_i \end{vmatrix} \end{array}$$

$$A =$$

Närvivõrgud

Hüpotees: närvivõrk toimib elektriliste signaalide abil.

Stiimul → retseptor → süsteem → efektor → reaktsioon

Ajus:

neuronite arv 10^{11}

sünaptiliste ühenduste arv 10^{14} – 10^{15}

ühel neuronil 5 – 10^{5} sünaptilist ühendust

närvirakud 5 – 100 μm

iseloomulik pikkuseskaala 10^{-4} mm

ajaskaala 1 ms

aksoni pikkus 0,1 mm – 1 m

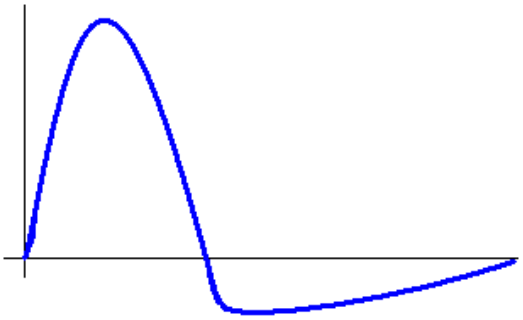

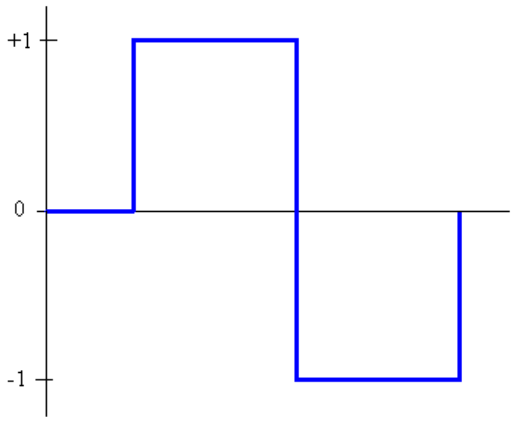

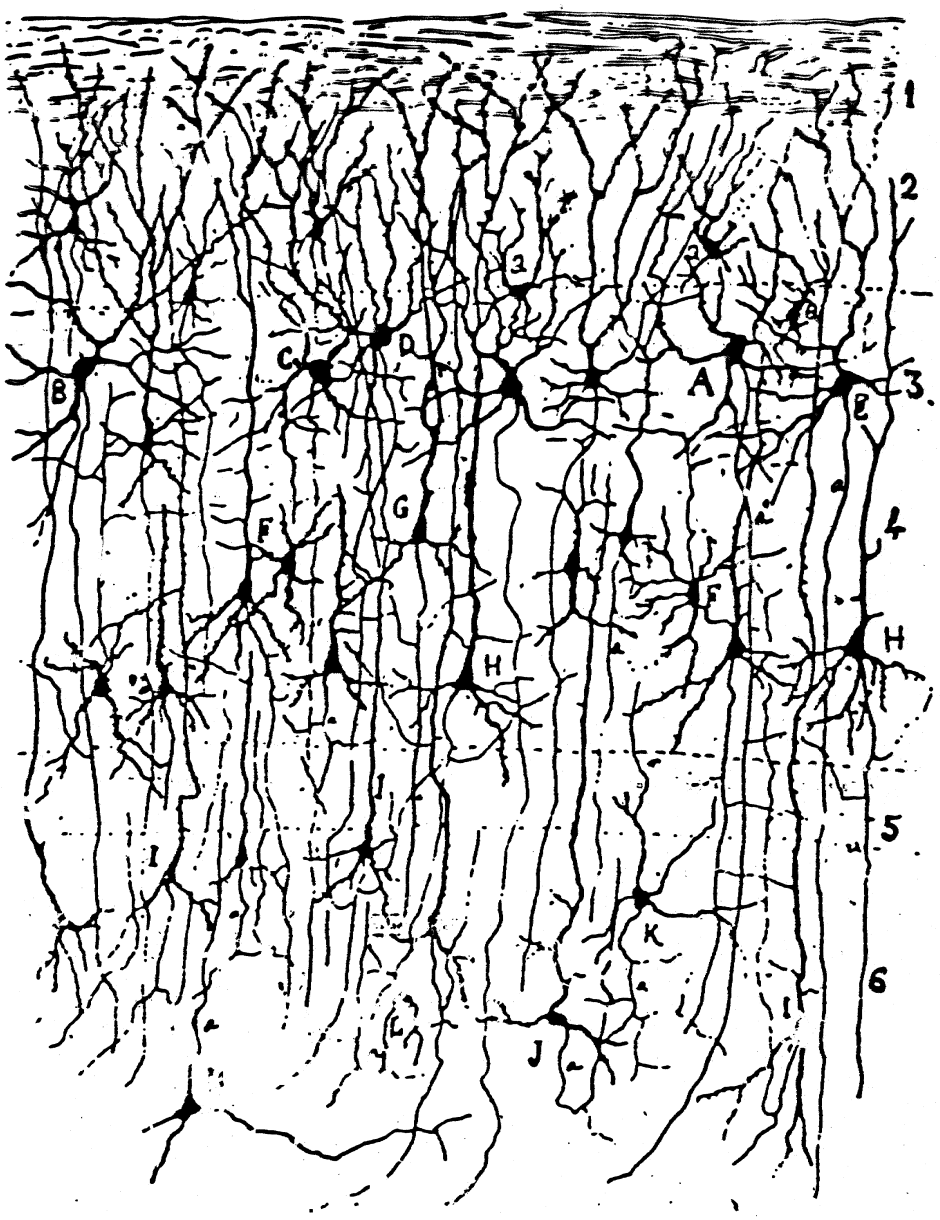

Figure 4.5.1. The complex ramified structure of typical nerve cells in the cerebral cortex is depicted.

Mc Cullochi ~ Pittsi neuron (1943)

1. Kõik või mitte midagi (all–or–none)
   muutuja σ_i

   $\sigma_i = +1$ aktiivne, $\sigma_i = -1$ mitteosalev

2. Stiimul neuronilt i neuronile j

   $V_{ij}(\sigma_j + 1)/2,$ $\quad \sigma_i = +1 \rightarrow V_{ij} \neq 0$, $\sigma_i = -1 \rightarrow V_{ij} = 0$

3. Lävi V_{oi}

4. Närvivõrgu olek

   $$\nu = \{\sigma_1(t), \sigma_2(t), \ldots \sigma_N(t)\}$$

5. Viiteaeg τ

   j aktiivne ajal t
   i tunneb stiimulit ajal $t + \tau$

6. Evolutsioon

   $$\sigma_i(t) = \operatorname{sgn}[F_i(t)],$$

   $$\operatorname{sgn}(x) = -1, \quad x < 0$$
   $$\operatorname{sgn}(x) = +1, \quad x \geq 0$$

   $$F_i(t) = \sum V_{ij}[\sigma_j(t - \tau) + 1]/2 - V_{oi} + [v_i]$$

   v_i välisärritus

   Hopfieldi neuron (1982)

13.3 Fraktalid

Fraktal – erinevatel mastaapidel enesesarnane kujund, mille dimensioon erineb täisarvust

Mandelbroti hulk – fraktaalne kujund

Looduslikud objektid:

pilved
puud
maapind
veresoonkond

Fraktalite konstrueerimise reeglid:

mitmekordne redutseeriv kopeerimine
(multiple reduction copy machine – MRCM)

itereeritud funktsioonid
(iterated function systems – IFS)

Vt. Ü. Lepik, J. Engelbrecht, Kaoseraamat.
TA Kirjastus, Tallinn, 1999

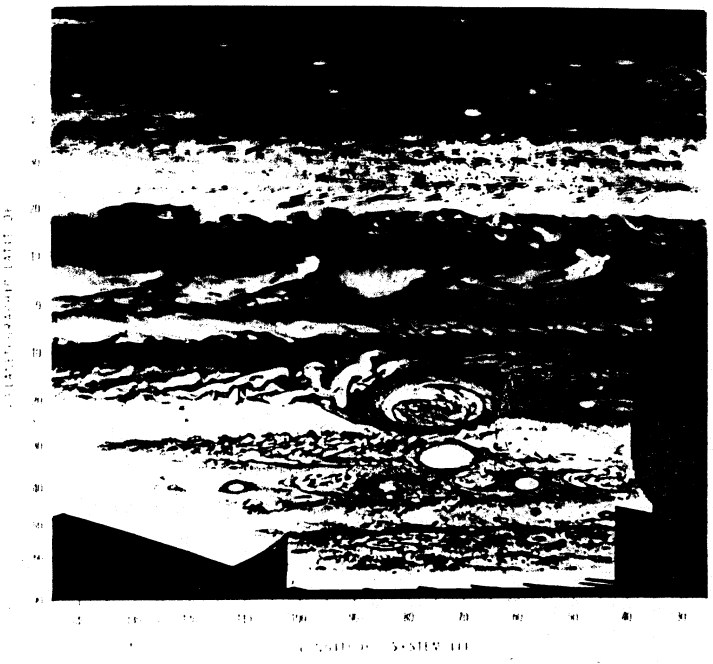

FIG. 3. North–south asymmetry in the Jovian cloud deck. This cylindrical map projection shows high latitude vortices, the White Oval BC below the Great Red Spot and three of the small white ovals at 40°. Combined with information from Tables I and II it can yield estimates of atmospheric parameters (NASA/JPL).

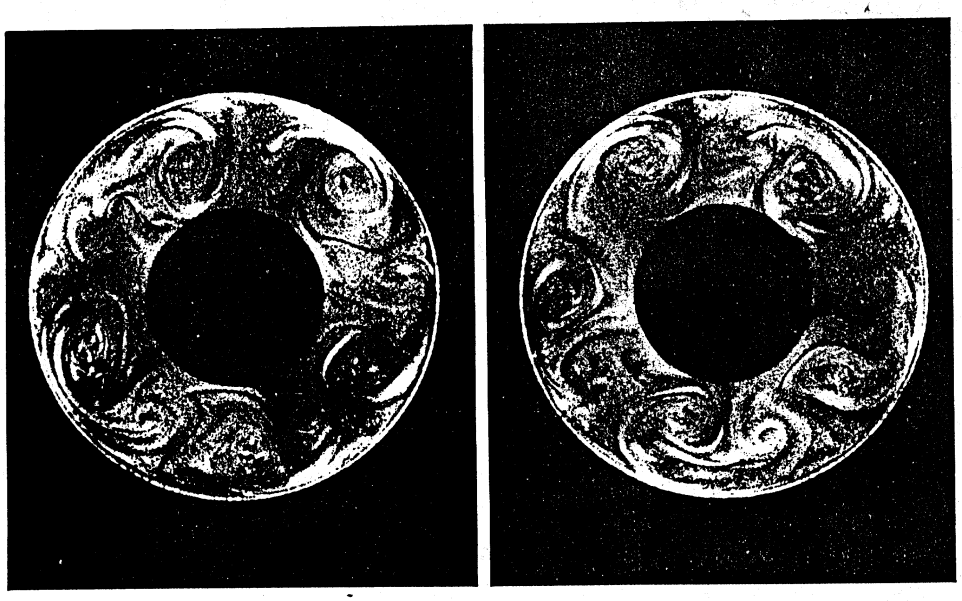

FIG. 14. Two photographs of time-dependent $m=5$ flows in an internally heated rotating annulus subject to strong internal heating (power input $=10^3$ W) and rapid rotation ($\Omega=4.45$ rad s^{-1}) (Ref. 27). Flows are illuminated at the upper level ($z/D=0.7$) and visualized using a suspension of aluminum powder in water.

Sile joon

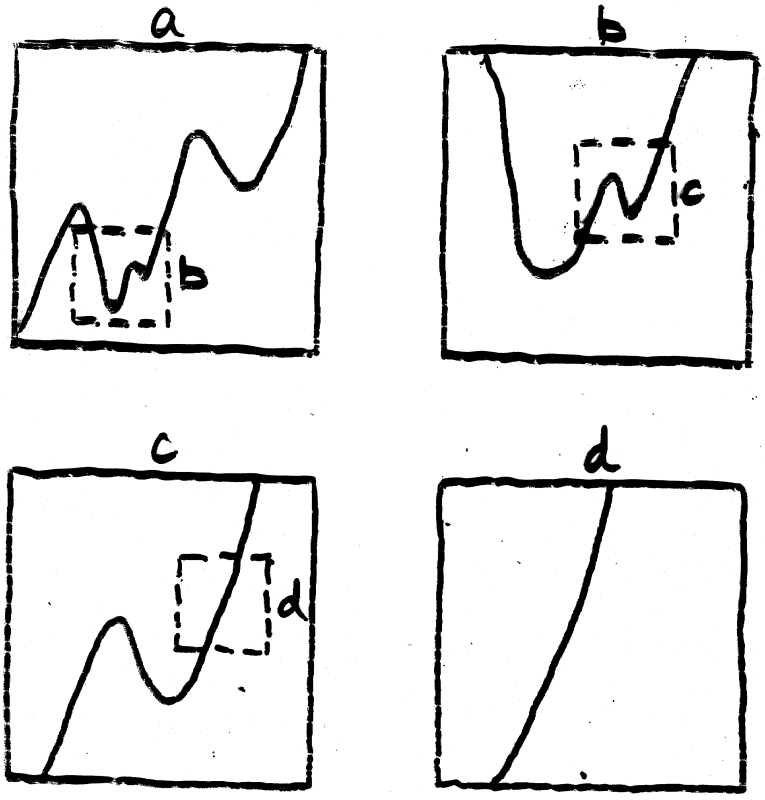

Fraktaalne joon

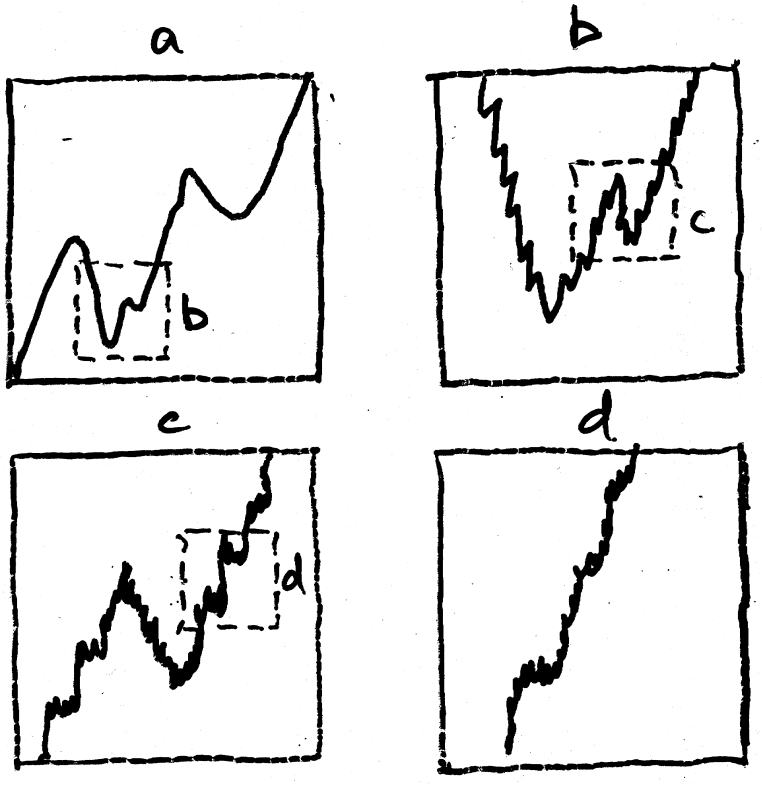

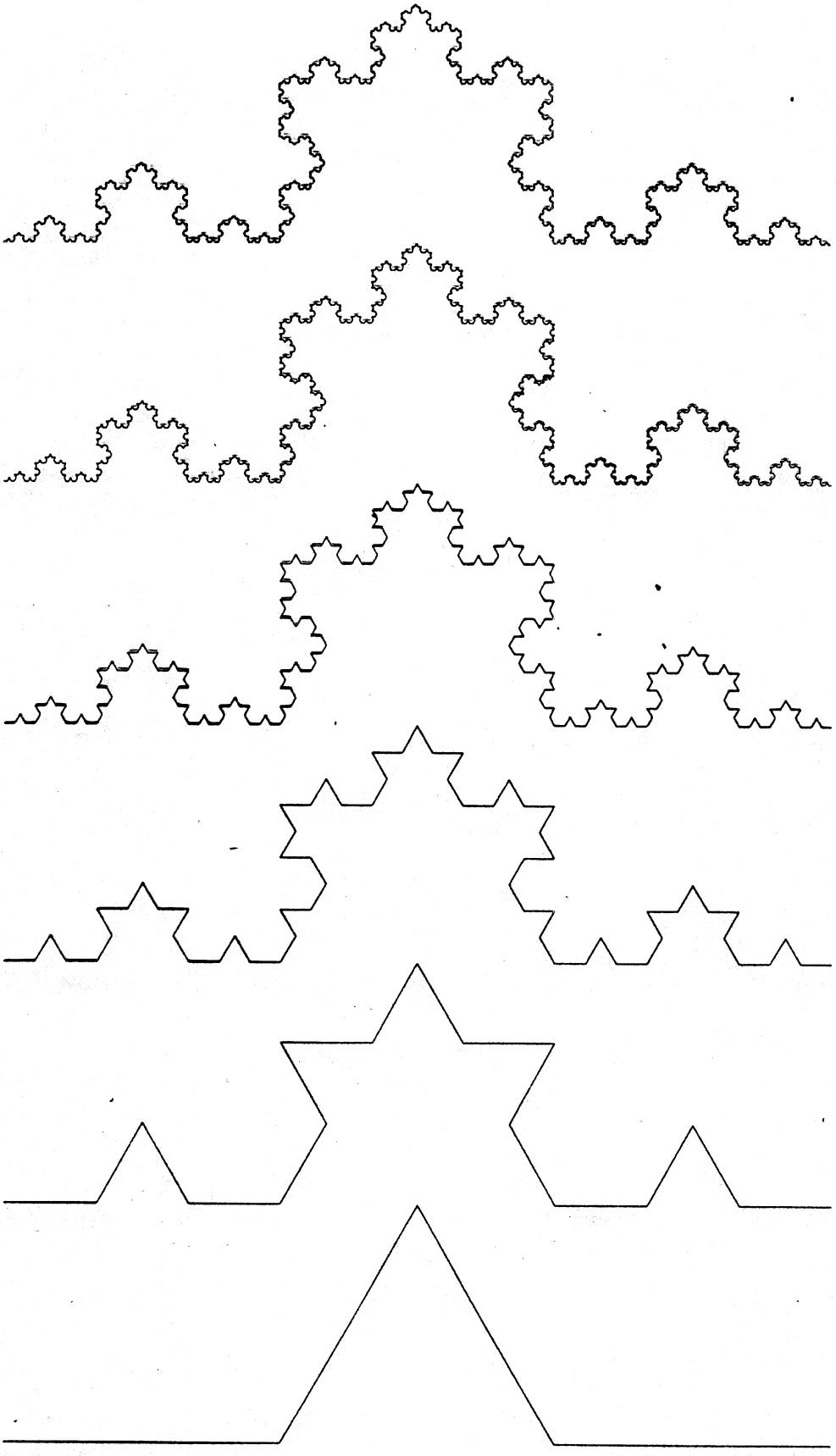

Fig. C.1: The first six stages in the generation of the von Koch snowflake curve. The 0L-system is given by the axiom "F", the angle $\delta = \frac{\pi}{3}$ and the production rule F → F−F++F−F.

Cauliflower Self-Similarity

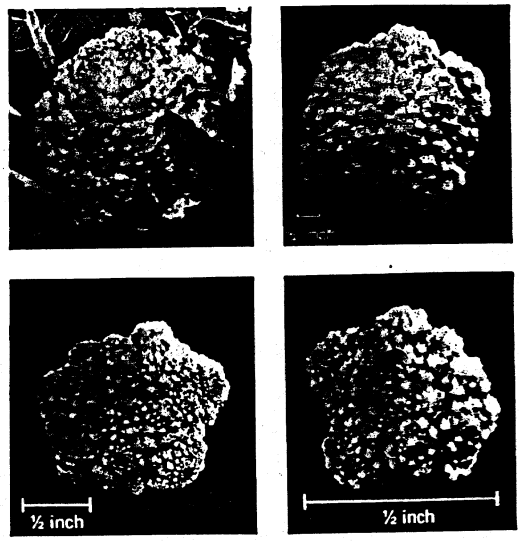

Figure 2.1 : The self-similarity of an ordinary cauliflower is demonstrated by dissection and two successive enlargements (bottom). The small pieces look similar to the whole cauliflower head.

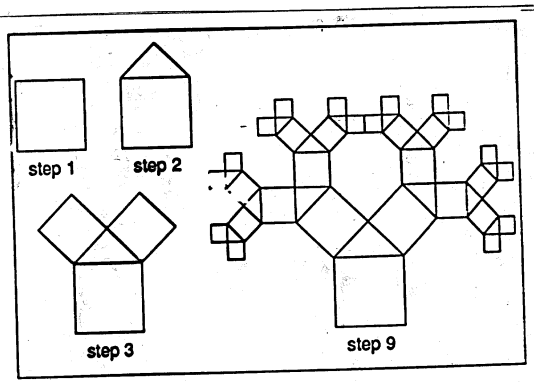

Figure 2.63 : Basic idea of a Pythagorean tree.

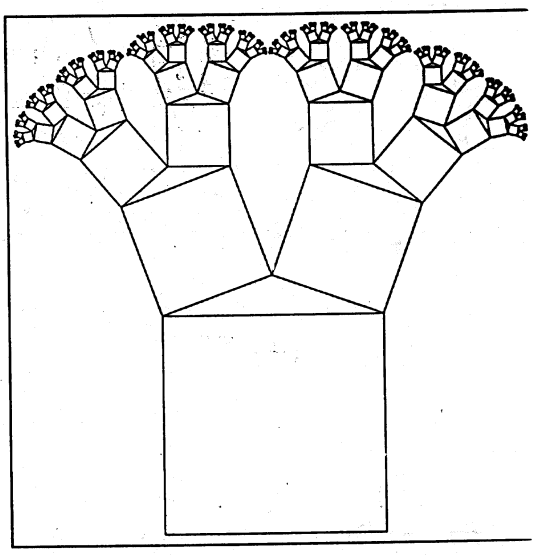

Figure 2.67 : Construction with isosceles triangles which hav angle greater than 90°

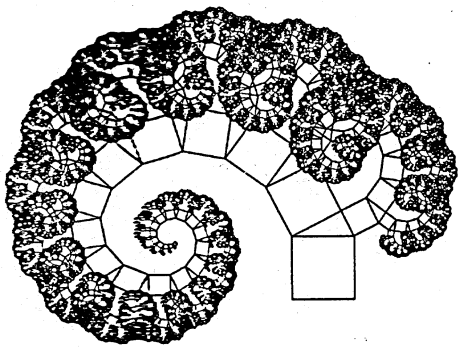

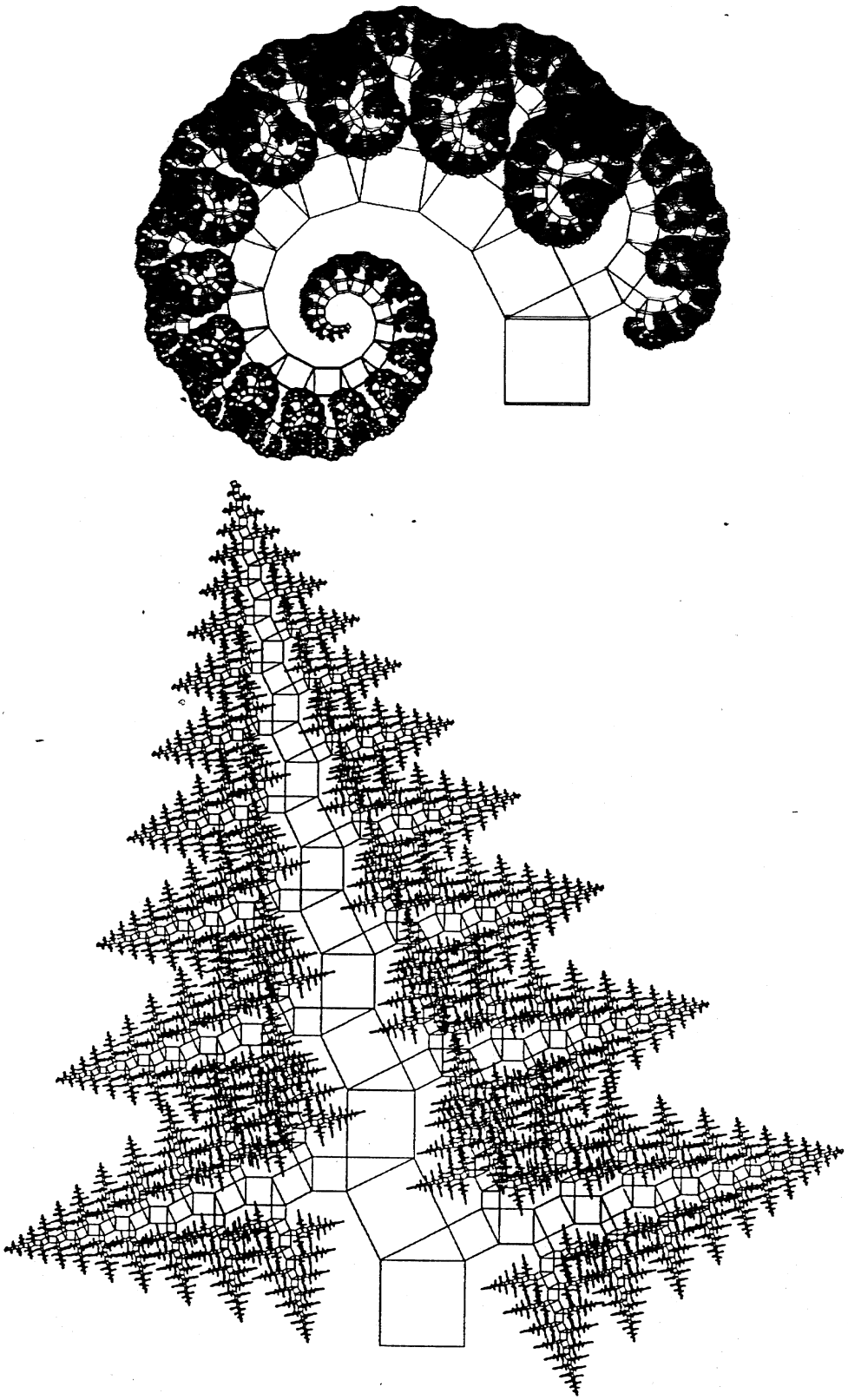

Figure 2.65 : The two constructions carried out some 50 times.
Note that the size of the triangles is the same in both.

Rectangle in MRCM

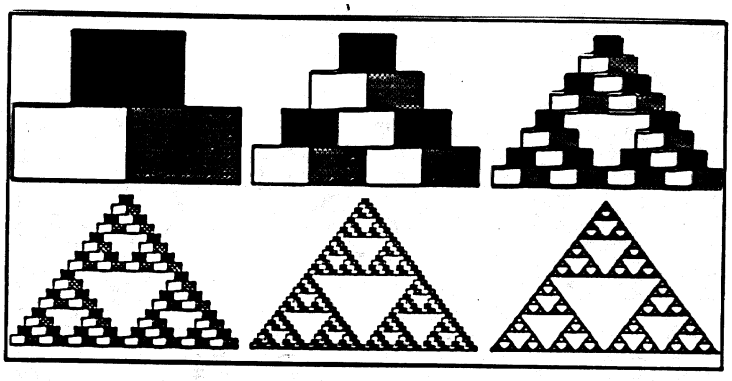

Figure 1.13 : Starting with a rectangle the iteration leads to the Sierpinski gasket. Shown are the first five steps and the result after some more iterations (lower right).

MRCM Applied to 'NCTM' and Other Shapes

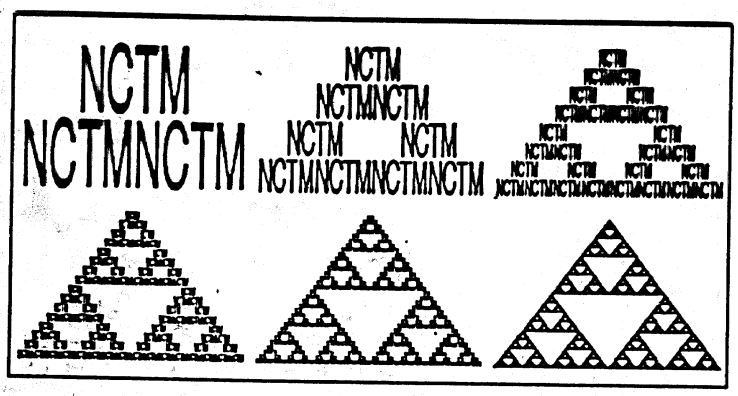

Figure 1.14 : We can start with an arbitrary image — this iterator will always lead to the Sierpinski gasket.

MRCM for the Sierpinski Gasket

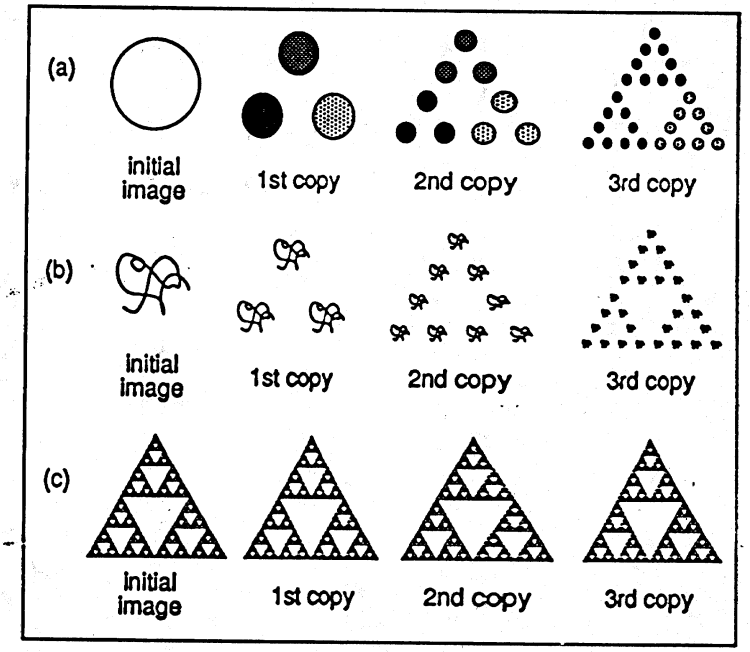

Figure 5.1 : Three iterations of an MRCM with three different initial images.

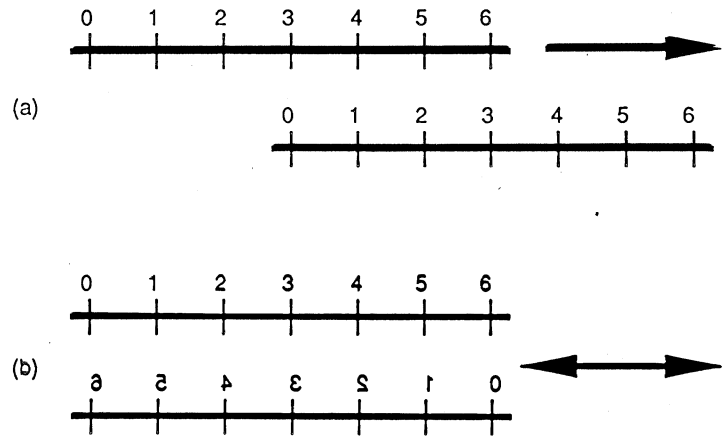

Figure 2.3 Symmetries of a line. (a) Translation. (b) Reflection

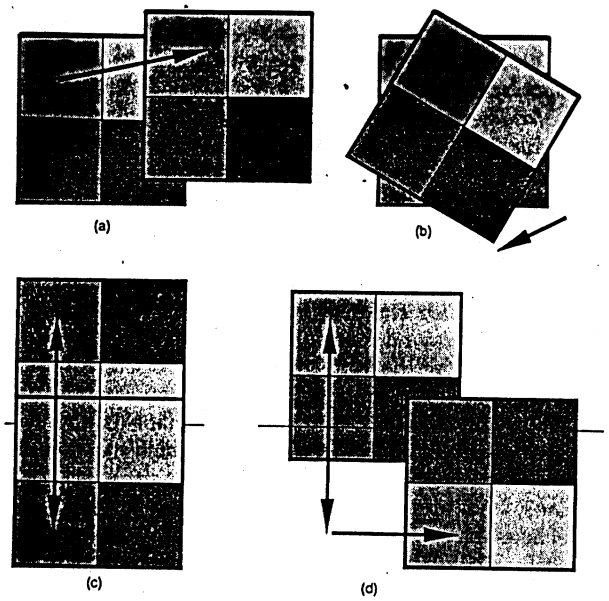

Figure 2.4 Symmetries of the plane. (a) Translation. (b) Rotation. (c) Réflection. (d) Glide reflection

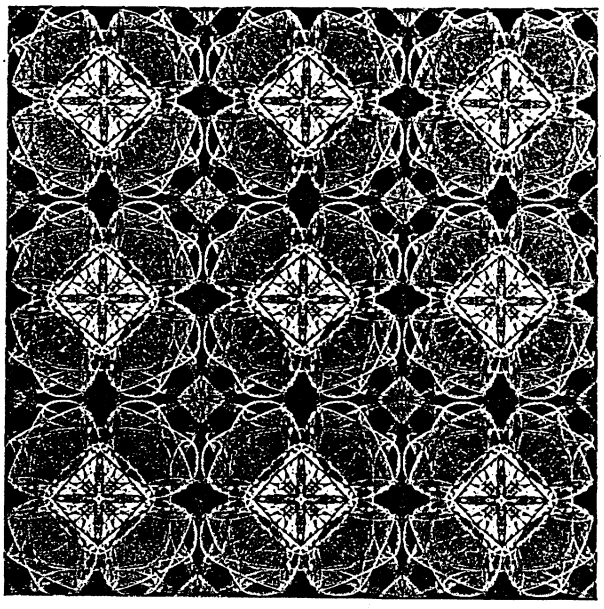

Blueprint of Barnsley's Fern

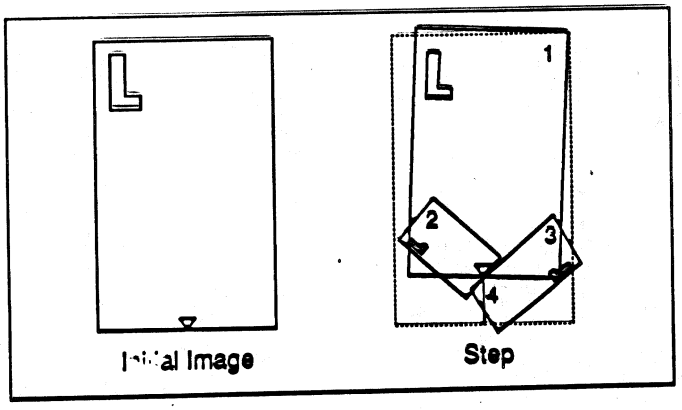

Figure 5.22 : Blueprint of Barnsley's fern.

Barnsley Fern Transformations

	Translations		Rotations		Scalings	
	e	f	θ	ψ	r	s
1	0.0	1.6	-2.5	-2.5	0.85	0.85
2	0.0	1.6	49	49	0.3	0.34
3	0.0	0.44	120	-50	0.3	0.37
4	0.0	0.0	0	0	0.0	0.16

Table 5.23 : Transformations for the Barnsley fern. The angles are given in degrees.

Barnsley's Fern

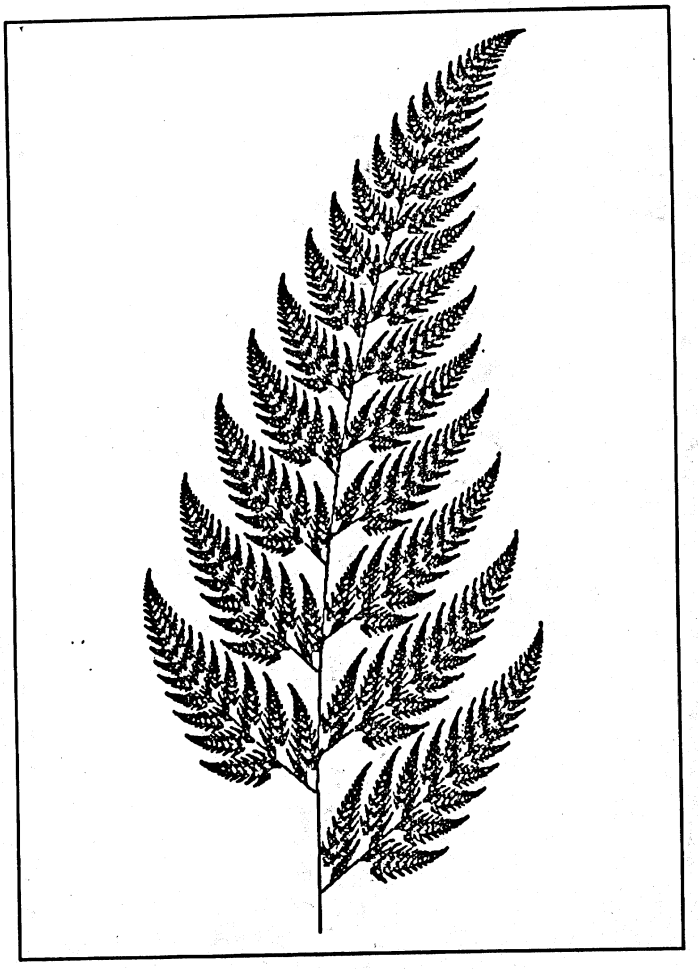

Figure 5.25 : Barnsley's fern generated by an MRCM with only four lens systems.

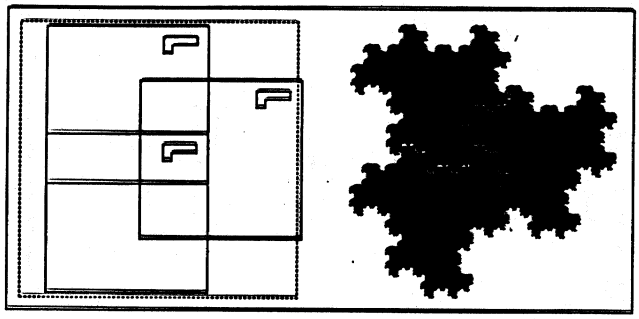

A Dragon With Threefold Symmetry

Figure 5.11 : The white line is inserted only to show that the figure can be made up from three parts similar to the whole.

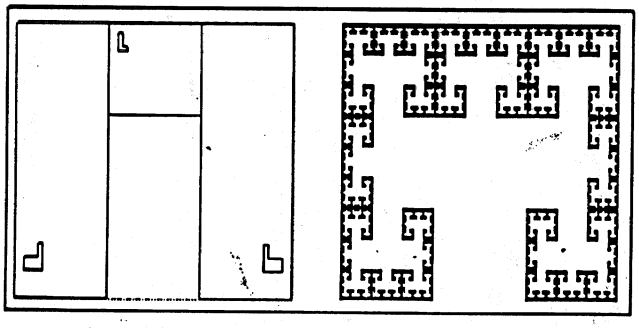

The Cantor Maze

Figure 5.12 : IFS with three transformations, one of which is a similarity. The attrcator is related to the Cantor set.

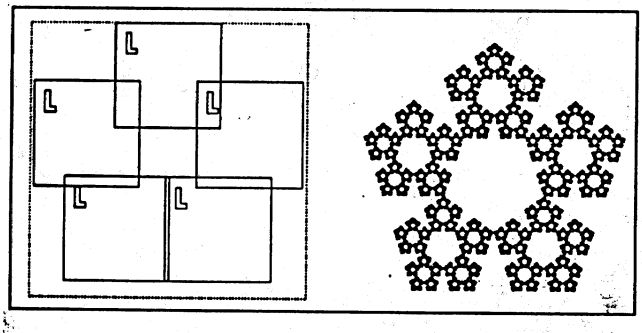

Crystal with Five Transformations

Figure 5.15 : IFS with five similarity transformations. Can you see Koch curves in the attractor?

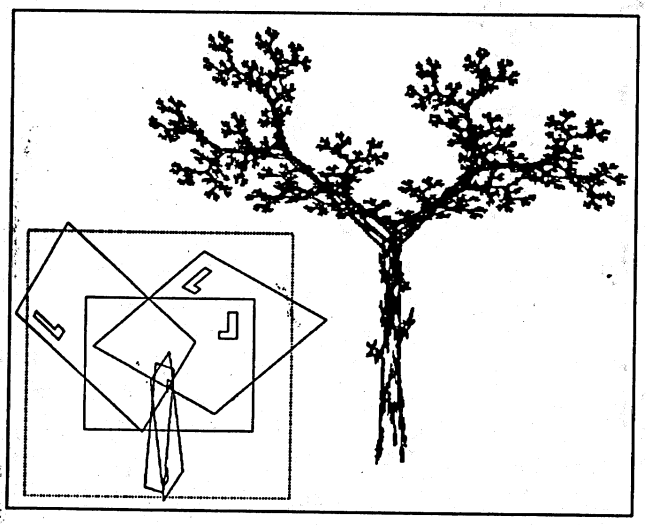

A Tree

Figure 5.16 : The attractor of an MRCM with five transformations can even resemble the image of a tree (the attractor is shown twice as large as the blue-print indicates).

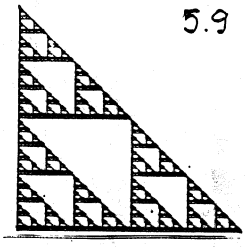

5.9

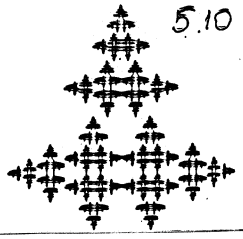

5.10

a	b	c	d	e	f
Figure 5.9					
0.500	0.000	0.00	0.500	0.0000	0.0000
0.500	0.000	0.00	0.500	0.5000	0.0000
0.500	0.000	0.00	0.500	0.0000	0.5000
Figure 5.10					
0.000	-0.500	0.500	-0.000	0.5000	0.0000
0.000	0.500	-0.500	0.000	0.5000	0.5000
0.500	0.000	0.000	0.500	0.2500	0.5000
Figure 5.11					
0.000	0.577	-0.577	0.000	0.0951	0.5893
0.000	0.577	-0.577	0.000	0.4413	0.7893
0.000	0.577	-0.577	0.000	0.0952	0.9893
Figure 5.12					
0.336	0.000	0.000	0.335	0.0662	0.1333
0.000	0.333	1.000	0.000	0.1333	0.0000
0.000	-0.333	1.000	0.000	0.0666	0.0000
Figure 5.13					
0.387	0.430	0.430	-0.387	0.2560	0.5220
0.441	-0.091	-0.009	-0.322	0.4219	0.5059
-0.468	0.020	-0.113	0.015	0.4000	0.4000
Figure 5.14					
0.255	0.000	0.000	0.255	0.3726	0.6714
0.255	0.000	0.000	0.255	0.1146	0.2232
0.255	0.000	0.000	0.255	0.6306	0.2232
0.370	-0.642	0.642	0.370	0.6356	-0.0061
Figure 5.15					
0.382	0.000	0.000	0.382	0.3072	0.6190
0.382	0.000	0.000	0.382	0.6033	0.4044
0.382	0.000	0.000	0.382	0.0139	0.4044
0.382	0.000	0.000	0.382	0.1253	0.0595
0.382	0.000	0.000	0.382	0.4920	0.0595
Figure 5.16					
0.195	-0.488	0.344	0.443	0.4431	0.2452
0.462	0.414	-0.252	0.361	0.2511	0.5692
-0.058	-0.070	0.453	-0.111	0.5976	0.0969
-0.035	0.070	-0.469	-0.022	0.4884	0.5069
-0.637	0.000	0.000	0.501	0.8562	0.2513
Figure 5.25					
0.849	0.037	-0.037	0.849	0.075	0.1830
0.197	-0.226	0.226	0.197	0.400	0.0490
-0.150	0.283	0.260	0.237	0.575	-0.0840
0.00	0.000	0.000	0.160	0.500	0.0000

Table 5.48 : Parameter table for the figures in this chapter.

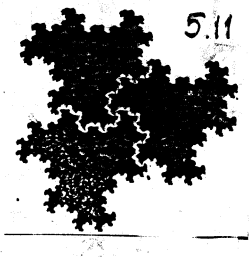

5.11

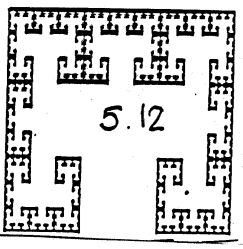

5.12

5.13

5.14

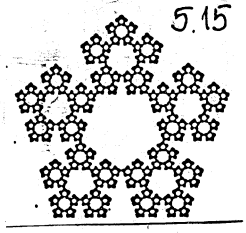

5.15

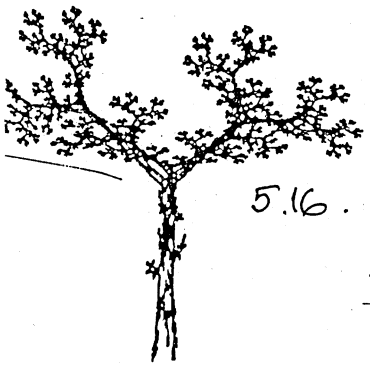

5.16.

5.25

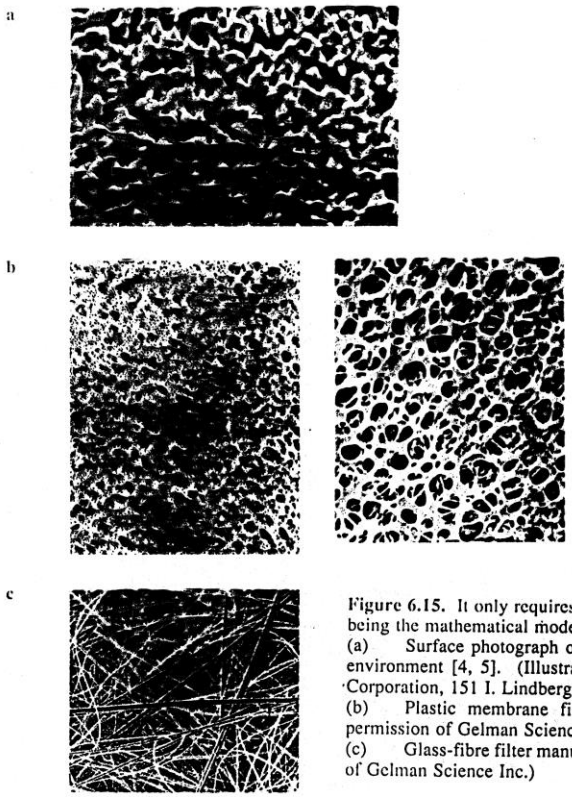

Figure 6.15. It only requires a small leap of the imagination to recognize Sierpinski carpets as being the mathematical model for filter systems.
(a) Surface photograph of a silver membrane filter used to filter quartz dust in a working environment [4, 5]. (Illustration provided by and used with the permission of The Poretics Corporation, 151 I. Lindbergh Avenue, Livermore, CA.)
(b) Plastic membrane filters manufactured by Gelman Science [6]. (Reproduced by permission of Gelman Science Inc.)
(c) Glass-fibre filter manufactured by Gelman Science Inc., [6]. (Reproduced by permission of Gelman Science Inc.)

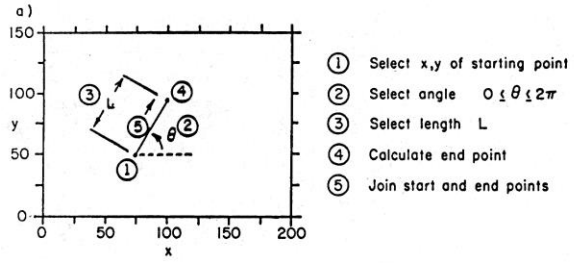

Figure 6.19. The structure of randomly assembled fibrous mats from short fibres, using a model similar to that first discussed by Clarenburg, can be simulated on the computer as illustrated above [10].
(a) Illustration of the construction algorithm followed in simulating short fibre felts.
(b) The appearance of 30-unit fibre length felts at various levels of population density.
(c) The appearance of felts at various population densities constructed from fibres of varying lengths.

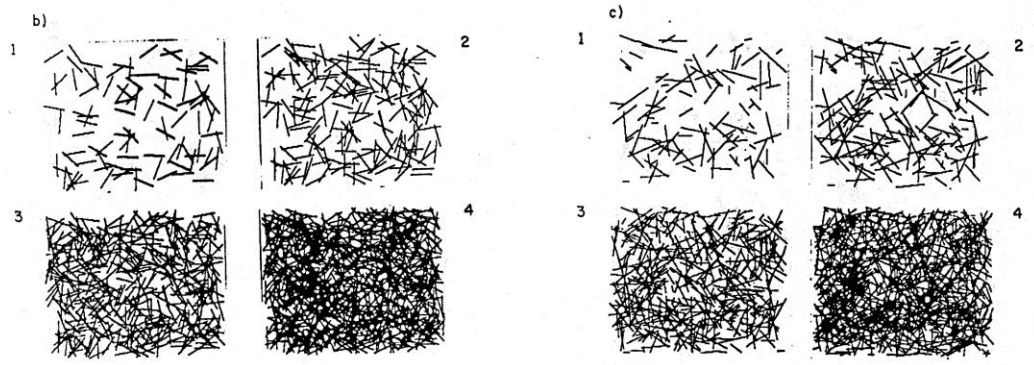

Kortsutatud paber

1. Katse

2. Teooria:
   - G. Gomper, Patterns of stress in crumpled paper. Nature, 1997, 386, 439-440
   - M. Ben Amar and Pomean, Crumpled paper, Proc. Royal Soc. London, 1997, 453, 729-755

3. Lahendusideed
   - leida pingefunktsioon, mis minimiseerib energia;
   - määrata kortsutatud pinna fraktaalsus.

4. Fullereenimolekul, jalgpall

$$\sigma_{xx} = \frac{\partial^2 \chi}{\partial y^2}, \quad \sigma_{yy} = \frac{\partial^2 \chi}{\partial x^2} \quad \text{and} \quad \sigma_{xy} = -\frac{\partial^2 \chi}{\partial x \partial y},$$

$$\frac{Eh^2}{24(1-\sigma^2)} \Bigg\{ -\frac{\partial \Delta \xi}{\partial n}$$
$$-(1-\sigma)\frac{\partial}{\partial l}\left[\cos(\theta)\sin(\theta)\left\{\frac{\partial^2 \xi}{\partial x^2} - \frac{\partial^2 \xi}{\partial y^2}\right\} + (\sin^2(\theta) - \cos^2(\theta))\frac{\partial^2 \xi}{\partial x \partial y}\right]\Bigg\}$$
$$+\left[\cos(\theta)\frac{\partial^2 \chi}{\partial y^2} - \sin(\theta)\frac{\partial^2 \chi}{\partial x \partial y}\right]\frac{\partial \xi}{\partial x} + \left[\sin(\theta)\frac{\partial^2 \chi}{\partial x^2} - \cos(\theta)\frac{\partial^2 \chi}{\partial x \partial y}\right]\frac{\partial \xi}{\partial y} = 0, \quad (2.4a)$$

$$\Delta \xi + (1-\sigma)\left[2\cos(\theta)\sin(\theta)\frac{\partial^2 \xi}{\partial x \partial y} - \sin^2(\theta)\frac{\partial^2 \xi}{\partial x^2} - \cos^2(\theta)\frac{\partial^2 \xi}{\partial y^2}\right] = 0, \quad (2.4b)$$

with

$$\sigma_{ij} n_j = P_i; \quad (2.4c)$$

θ means the angle between the x axes and the normal to the boundary, $\partial/\partial l$ (resp. $\partial/\partial n$) is the derivative with respect to the arclength (resp. the normal coordinate) along the boundary. These boundary conditions have to be verified for the freely hanging part of the plate where ξ and its derivatives can be arbitrary. For clamped sides of the plates, only (2.4 c) remains valid, while for simply supported part, one can forget (2.4 a). Let us also notice that one can get rid of the Young modulus E in (2.3 b) and (2.4 a), (2.4 b) by redefining a scaled Airy potential $\chi' = \chi/E$, so that the functional to be minimized becomes

$$F'\{\xi, \chi'\} = h \int_\Omega dx\, dy \Bigg\{ \frac{h^2}{24(1-\sigma^2)}\{(\nabla^2 \xi)^2 - 2(1-\sigma)[\xi, \xi]\}$$
$$+\tfrac{1}{2}(\nabla^2 \chi')^2 - (1+\sigma)[\chi', \chi']\Bigg\}. \quad (2.5a)$$

The Buckyball Molecule

Today, the truncated icosahedron is an exceptionally important polyhedron due to the recently discovered C_{60} molecule called *buckminsterfullerene*, or in short, buckyball. Many names were proposed for this newly discovered substance. One of them in Europe was "footballene." However, what Europeans call football, Americans call soccer, so in the United States this would have to be translated as "soccerene."

The molecule was named after R. Buckminster (Bucky) Fuller, the inventor and designer who used icosahedral geometry as the basis for his geodesic domes.

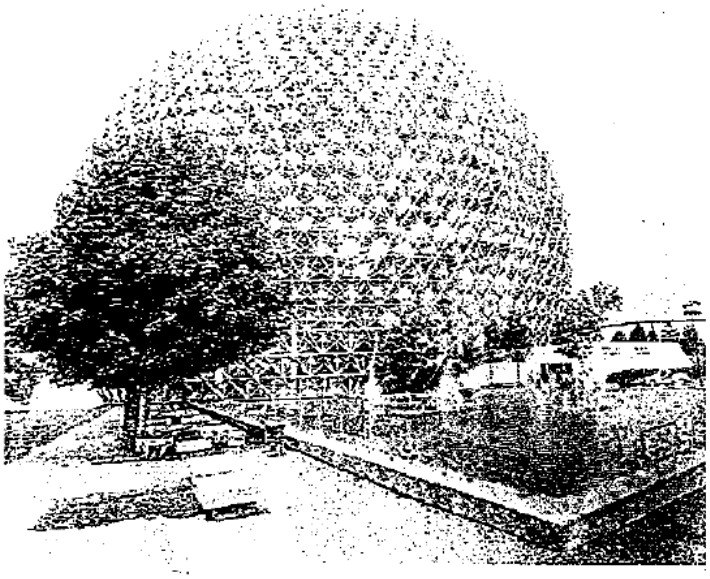

ABOVE: *R. Buckminster Fuller's geodesic dome at the Montreal Expo in 1967*

LEFT: *R. Buckminster Fuller (1895–1983) at Pacific High School, Saratoga, California, 1970*

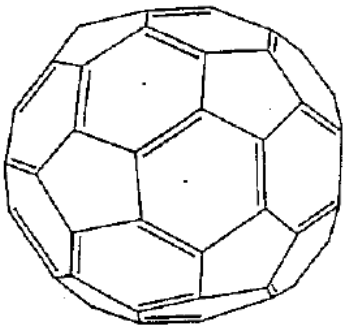

The structure of the superstable C_{60} molecule in which the tetravalency of all carbon atoms is neatly maintained

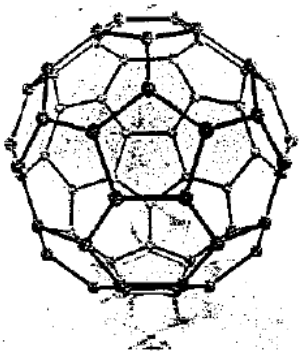

ABOVE: *Truncated icosahedron model made with Steve Baer's Zometool model kit*

Ivory Coast stamp honoring the football world championship, Argentina, 1978

Figure 6. (a) Schematic representation (front view) of the woven "sepak raga" ball; (b) Schematic representation of the modern soccer ball structure; (c) The "sepak raga"—soccer ball structure of buckminsterfullerene.

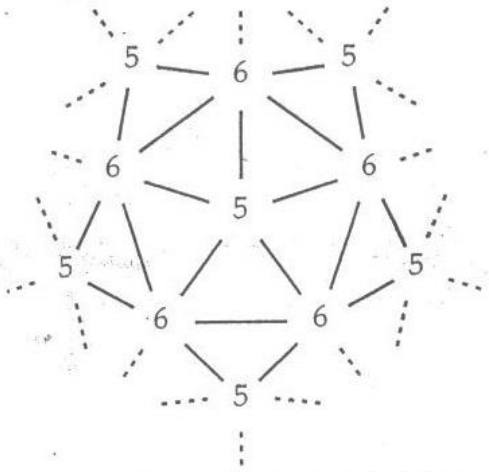

Figure 20. Hexastrip numbering scheme for the top half of a C_{120} isomer. The numbers 5 and 6 represent pentagonal and hexagonal holes.

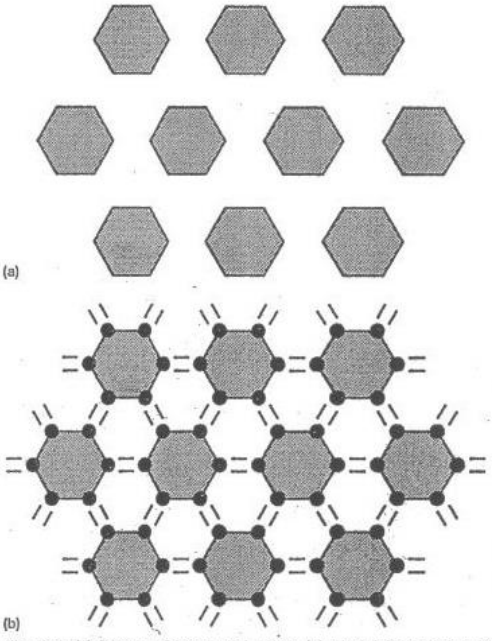

Figure 3. (a) Pattern of hexagonal holes; (b) Model for a layer of graphite.

Näide: Crumpled paper

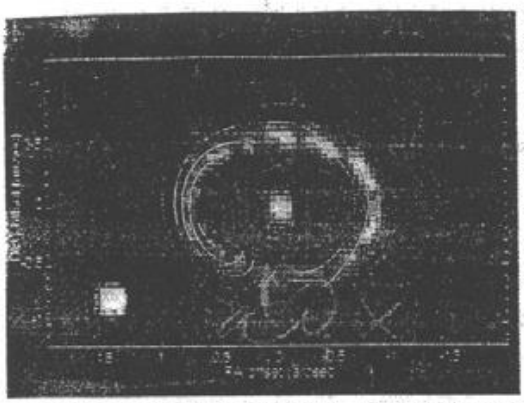

Figure 1 Radio and optical images of SN1987A and its inner ring[7]. The bright radio lobes seen at 9 GHz (contour lines) are synchrotron radiation from relativistic electrons accelerated by the supernova blast wave, which is now nearing the inner circumstellar ring.

has given us a good picture of the structure and thermodynamics of the explosion debris (C. Fransson, Stockholm Obs.). After the explosion, the debris was mixed on large scales by instabilities, but it has remained chemically inhomogeneous. The observed degree of mixing requires that the supernova progenitor was asymmetric, possibly owing to strong convection driven by thermonuclear burning (D. Arnett, Univ. Arizona).

The debris is now very cold throughout. Less than two years after the explosion, the iron-rich and oxygen-rich components cooled by radiation to a few hundred K (the thermal catastrophe), and now even the helium- and hydrogen-rich components have cooled, by adiabatic expansion[1]. Today, the optical emission from the supernova debris is dominated by recombination of residual hydrogen ions and atomic excitation resulting from the radioactive decay of about 10^{-4} solar masses of ^{44}Ti.

Why was the progenitor of SN1987A a blue supergiant star rather than a red supergiant, as is thought to be the case for most type-II supernovae? Perhaps, as the binding energy of a massive star is insensitive to the radius of its outer envelope, subtle changes in the opacity or mean molecular weight of the envelope allowed it to shrink, heating it and changing its colour from red to blue (S. Woosley, Univ. Calif. Santa Cruz).

Another model that leads to a blue supergiant is one in which the progenitor formed from the merger of two stars in a binary system[2]. Evidence in favour of the merged binary hypothesis comes from Hubble Space Telescope images of SN1987A. They show a bright ring around the star[3,4] (Fig. 1), which can be explained as a real physical ring, ejected as an equatorial outflow of several solar masses of gas during a merger of the two stars some 20,000 years before the explosion. Such a merger would probably yield a progenitor that is highly flattened by rotation. If so, the explosion would naturally blow out preferentially along the polar axis, as indicated by recent images showing that the glowing debris of the supernova itself is elongated perpendicular to the ring plane (J. Pun, NASA/Goddard). But although such a model may be plausible, it is not well developed, and certainly not universally accepted. Moreover, it does not provide a simple explanation for the origin of the outer circumstellar loops. The inner ring and the outer loops are more probably thin, flash-ionized layers at the inner surfaces of a much greater mass of circumstellar matter, as yet unseen.

When SN1987A aficionados converge again to celebrate its 20th anniversary, we should have a good chance to unravel some of its mysteries. The blast wave from the supernova will strike the inner ring some six to ten years from now[5,6]. When it does, the resulting shock wave will cause the ring to brighten by a factor ~ 10^3 in all bands of the electromagnetic spectrum (except γ-rays). The ionizing radiation from the interaction will illuminate hitherto unseen circumstellar matter. Moreover, the impact will give us an unprecedented experiment in the physics of interstellar shocks, including a chance to observe the acceleration of relativistic electrons in real time.

In fact, we are already seeing precursors of this impact, in non-thermal radio emission seen by the Australia Telescope Compact Array[7] and X-ray emission seen by ROSAT[8]. Evidently, the supernova blast has already encountered a region of relatively dense ionized hydrogen inside the inner ring[2]. Although we don't yet have a clear picture of this shock, a model for the X-ray emission[6] suggests that the shocked gas should be bright enough in ultraviolet emission lines to see with the Space Telescope Imaging Spectrometer that was installed during the last Hubble Space Telescope servicing mission. If so, we should soon have images and spectra of sufficient quality to locate the blast wave and tell us when it will strike the ring. □

Richard McCray is in the Department of Astrophysical and Planetary Sciences, University of Colorado, Boulder, Colorado 80309-0440, USA.

1. Wang, L. *et al. Astrophys. J.* 466, 998–1010 (1996).
2. Podsiadlowski, P. *Publ. Astron. Soc. Pacif.* 104, 717–729 (1992).
3. Blondin, J. M. & Lundqvist, P. *Astrophys. J.* 405, 337–352 (1993).
4. Martin, C. L. & Arnett, D. *Astrophys. J.* 447, 378–390 (1995).
5. Chevalier, R. A. & Dwarkadas, V. V. *Astrophys. J.* 452, L45–L48 (1995).
6. Borkowski, K., Blondin, J. & McCray, R. *Astrophys. J.* 476, L31–L34 (1997).
7. Gaensler, B. M. *et al. Astrophys. J.* (in the press).
8. Hasinger, G., Aschenbach, B. & Trumper, J. *Astron. Astrophys.* 312, L9–L12 (1996).

Mechanics

Patterns of stress in crumpled sheets

Gerhard Gompper

The forced crumpling of thin elastic sheets is experienced frequently in everyday life. Typical examples are the crumpling of paper — which is particularly familiar to scientists — the crumpling of soda cans after use, and the crumpling of metal sheets in car accidents. Despite the enormous importance of this phenomenon, our understanding of the behaviour of strongly deformed elastic sheets is limited. In a paper published on 17 February in *Physical Review Letters*, Kramer and Witten[1] demonstrate for the first time that a large part of the total elastic energy of a crumpled sheet is contained in a network of narrow, stretching ridges. This result could open the door, for example, to the rational design of energy-absorbing materials.

It all began with the attempt by Witten and Li[2] to understand the shape of very large fullerene balls. In the limit of large size, deformation can be described by continuum elastic theory. There are two contributions to the elastic energy: the stretching energy, which is the cost of changing the bond length of neighbouring carbon atoms from minimum-energy values; and the bending energy, which describes the energy cost of tilting adjacent carbon rings with respect to one another. If there were no energy cost to bend the surface, the stable shape of the molecule would be a regular, flat-sided icosahedron (with a carbon pentagon at each of the twelve corners) — a shape that requires no bond stretching. When the bending rigidity is finite, however, the sharp edges of the icosahedron are expected to soften so that the minimum-energy surface is smooth except near the corners.

One of the appealing features of this kind of research is that many effects can be seen qualitatively in simple 'paper experi-

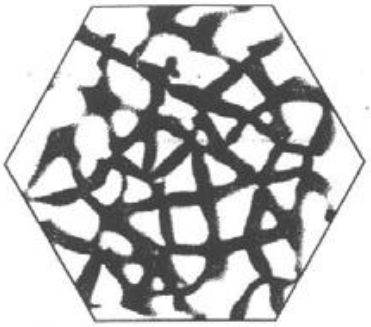

Figure 1 Curvature energy distribution in a hexagonal sheet of diameter L, which has been crushed into a sphere of radius $R_0 \approx L/6$. Darker regions have higher energy density. (From ref. 1.)

ments[1,2,4]. I would therefore like to encourage readers to study the geometry shown in the panel (below) with a sheet of paper. It can be easily seen in such an experiment that the curvature is localized near the ridge that connects two opposing corners.

Witten and Li[2] give a very simple argument for the shape of the edge connecting two corners, and the dependence of edge energy on scale (see panel). The simplicity of their argument means that it has had to be checked carefully to test its validity and its range of applicability. This has been done by computer simulations of simple models of triangulated surfaces, which were introduced some time ago by Kantor and Nelson[5]. The numerical studies, carried out by Witten and co-workers[4] and by Kroll and co-workers[6], show that the scaling laws do indeed describe the asymptotic behaviour of large fullerene balls. However, quite large system sizes are necessary in order to observe this behaviour, with edge lengths 1,000 times the effective thickness of the sheet or more. For smaller systems, such as C_{60}, the bending energy of the cone-shaped regions near the corners dominates[4,6].

Kramer and Witten[1] have now gone beyond the study of isolated stretching ridges. In their computer simulation, a nearly flat sheet is approximated by a triangular network of springs with some bending elasticity. They put the sheet into a spherical shell, and slowly decrease the shell radius R_0 until it is much smaller than the diameter L of the initial sheet. The resulting distribution of the curvature energy is shown in Fig. 1. It clearly demonstrates the formation of stretching ridges. About 40% of the energy is localized in very small areas (vertices), which correspond to the corners of the fullerene balls; the next 40% is contained in the narrow ridges that connect the vertices. Since the length of each ridge is found to be similar to the radius R_0 of the confining sphere, their number must go as $(L/R_0)^2$, so the total elastic energy should scale as $R_0^{-5/3}$ (see panel). The simulation results are consistent with this prediction.

The theory of crumpled sheets applies to macroscopic as well as to microscopic elastic sheets. The work of Witten and co-workers[1,2,4], which led to the present understanding of the crumpled state, originated in studies of the properties of fluid and polymer membranes[7,8]. For these microscopic surfaces, thermal fluctuations can be important. It has been shown, for example, that thermal fluctuations crumple non-self-avoiding polymerized membranes with small bending rigidities[5] without any external compression. And fluid membranes, which have no stretching energy, collapse into crumpled, branched-polymer-like shapes for sufficiently low bending rigidity due to thermal fluctuations[9], even with self-avoidance.

But self-avoidance stabilizes the flat phase[10] in all real polymerized membranes, such as graphite-oxide sheets[11] or the spectrin network of red blood cells[12], giving them the elastic stiffness relevant to the new study. Further, thermal fluctuations should not modify the scaling behaviour of stretching ridges[13]. So knowledge about ridges may help us understand the passage of red blood cells through narrow capillaries[14], for example.

It is the subtle interplay between stretching, bending and thermal fluctuations which makes this field so exciting, and which gives microscopic membranes their unique properties. The work of Kramer and Witten is a beautiful example of the contribution that physics can make to materials research and mechanical engineering, and it should have important implications for the understanding of biological systems. □

Gerhard Gompper is in the Max-Planck-Institut für Kolloid- und Grenzflächenforschung, Kantstrasse 55, 14513 Teltow, Germany.

1. Kramer, E. M. & Witten, T. A. *Phys. Rev. Lett.* **78**, 1303–1306 (1997).
2. Witten, T. A. & Li, H. *Europhys. Lett.* **23**, 51–55 (1993).
3. Kantor, Y., Kardar, M. & Nelson, D. R. *Phys. Rev. A* **35**, 3056–3071 (1987).
4. Lobkovsky, A., Gentges, S., Li, H., Morse, D. & Witten, T. A. *Science* **270**, 1482–1485 (1995).
5. Kantor, Y. & Nelson, D. R. *Phys. Rev. Lett.* **58**, 2774–2777 (1987); *Phys. Rev. A* **36**, 4020–4032 (1987).
6. Zhang, Z., Davis, H. T., Maier, R. S. & Kroll, D. M. *Phys. Rev. B* **52**, 5404–5413 (1995).
7. Nelson, D., Piran, T. & Weinberg, S. (eds) *Statistical Mechanics of Membranes and Surfaces* (World Scientific, Singapore, 1989).
8. Lipowsky, R. *Nature* **349**, 475–481 (1991).
9. Gompper, G. & Kroll, D. M. *Phys. Rev. Lett.* **73**, 2138–2141 (1994); *Phys. Rev. E* **51**, 514–525 (1995).
10. Abraham, F. F., Rudge, W. E. & Plischke, M. *Phys. Rev. Lett.* **62**, 1757–1759 (1989).
11. Spector, M. S., Naranjo, E., Chiruvolu, S. & Zasadzinski, J. A. *Phys. Rev. Lett.* **73**, 2867–2870 (1994).
12. Schmidt, C. F. *et al. Science* **259**, 952–955 (1993).
13. Zhang, Z., Davis, H. T. & Kroll, D. M. *Z. Phys. B* **97**, 337–340 (1995).
14. Reinhart, W. H. *et al. Biorheology* **28**, 537–549 (1991).

Scaling ridges

Witten and Li[2] give a very simple scaling argument for the shape of the edge connecting two corners of an elastic icosahedron, depicted in the figure here. Any deformation that involves most of the bonds on the surface costs an energy proportional to the area; therefore, stretching has to be confined to narrow ridges along the edges. The surface near the edge is now assumed to have a roughly cylindrical shape, with a radius of curvature $R_\perp$ at its midpoint. For a distance R between the corners, the total curvature energy is approximately $\kappa A R_\perp^{-2}$,

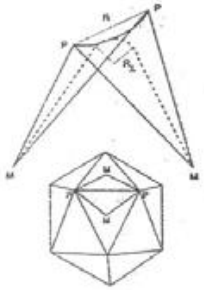

where κ is the bending rigidity and $A \approx R R_\perp$ is the area of the curved region. The curvature of the edge implies that the mid-line of the bend retracts inward. Because the distance R cannot change (this would require the faces of the icosahedron to be compressed, at a prohibitively large cost in stretching energy), the length of the mid-line must therefore increase by a fraction of order $\gamma \approx (R_\perp/R)^2$. The fraction γ is proportional to the change of the carbon–carbon bond length along the ridge, so the bond stretching energy is about $K_0 A \gamma^2$, where K_0 is the bond's elastic modulus. Minimization of the total energy then gives the result that the radius of the edge curvature scales as $R_\perp \approx R^{2/3}$, and the total edge energy as $\sim R^{1/3}$. So for large R, the curvature is indeed concentrated into narrow (small $R_\perp$) ridges. **GG**